remote sensing

MDPI

Article

Mapping Water Levels across a Region of the Cuvette Centrale Peatland Complex

Selena Georgiou [1,*], Edward T. A. Mitchard [1], Bart Crezee [2], Greta C. Dargie [2], Dylan M. Young [2], Antonio J. Jovani-Sancho [3], Benjamin Kitambo [4,5,6], Fabrice Papa [4,7], Yannick E. Bocko [8], Pierre Bola [9], Dafydd E. Crabtree [3], Ovide B. Emba [9], Corneille E. N. Ewango [10], Nicholas T. Girkin [11], Suspense A. Ifo [8], Joseph T. Kanyama [10], Yeto Emmanuel Wenina Mampouya [8], Mackline Mbemba [8], Jean-Bosco N. Ndjango [10], Paul. I. Palmer [1,12], Sofie Sjögersten [13] and Simon L. Lewis [2,14]

1 School of GeoSciences, King's Buildings, University of Edinburgh, Edinburgh EH9 3JN, UK
2 School of Geography, University of Leeds, Leeds LS2 9JT, UK
3 UK Centre for Ecology & Hydrology, Bangor LL57 2UW, UK
4 LEGOS, Université de Toulouse, IRD, CNES, CNRS, UPS, 31400 Toulouse, France
5 Congo Basin Water Resources Research Center (CRREBaC), Department of Natural Resources Management, University of Kinshasa (UNIKIN), Kinshasa BP 190, Democratic Republic of the Congo
6 Faculty of Sciences, Department of Geology, University of Lubumbashi (UNILU), Route Kasapa, Lubumbashi BP 1825, Democratic Republic of the Congo
7 Instituto de Geociências, IRD, Universidade de Brasília (UnB), Brasília 70297-400, Brazil
8 Laboratoire de Botanique et Ecologie, Faculté des Sciences et Techniques, Université Marien Ngouabi, Brazzaville BP 69, Democratic Republic of the Congo
9 Département de Biologie, Géographie et Gestion de l'environnement, Institut Supérieur Pédagogique de Mbandaka, Mbandaka BP 116, Democratic Republic of the Congo
10 Faculté de Gestion des Ressources Naturelles Renouvelables, Université de Kisangani, Kisangani BP 2012, Democratic Republic of the Congo
11 School of Water, Energy and Environment, Cranfield University, Cranfield MK43 0JR, UK
12 National Centre for Earth Observation, University of Edinburgh, Edinburgh EH9 3JN, UK
13 School of Biosciences, University of Nottingham, Loughborough LE12 5RD, UK
14 Department of Geography, University College London, London WC1E 6BT, UK
* Correspondence: selena.georgiou@ed.ac.uk

Abstract: Inundation dynamics are the primary control on greenhouse gas emissions from peatlands. Situated in the central Congo Basin, the Cuvette Centrale is the largest tropical peatland complex. However, our knowledge of the spatial and temporal variations in its water levels is limited. By addressing this gap, we can quantify the relationship between the Cuvette Centrale's water levels and greenhouse gas emissions, and further provide a baseline from which deviations caused by climate or land-use change can be observed, and their impacts understood. We present here a novel approach that combines satellite-derived rainfall, evapotranspiration and L-band Synthetic Aperture Radar (SAR) data to estimate spatial and temporal changes in water level across a sub-region of the Cuvette Centrale. Our key outputs are a map showing the spatial distribution of rainfed and flood-prone locations and a daily, 100 m resolution map of peatland water levels. This map is validated using satellite altimetry data and in situ water table data from water loggers. We determine that 50% of peatlands within our study area are largely rainfed, and a further 22.5% are somewhat rainfed, receiving hydrological input mostly from rainfall (directly and via surface/sub-surface inputs in sloped areas). The remaining 27.5% of peatlands are mainly situated in riverine floodplain areas to the east of the Congo River and between the Ubangui and Congo rivers. The mean amplitude of the water level across our study area and over a 20-month period is 22.8 ± 10.1 cm to 1 standard deviation. Maximum temporal variations in water levels occur in the riverine floodplain areas and in the inter-fluvial region between the Ubangui and Congo rivers. Our results show that spatial and temporal changes in water levels can be successfully mapped over tropical peatlands using the pattern of net water input (rainfall minus evapotranspiration, not accounting for run-off) and L-band SAR data.

check for updates

Citation: Georgiou, S.; Mitchard, E.T.A.; Crezee, B.; Dargie, G.C.; Young, D.M.; Jovani-Sancho, A.J.; Kitambo, B.; Papa, F.; Bocko, Y.E.; Bola, P.; et al. Mapping Water Levels across a Region of the Cuvette Centrale Peatland Complex. *Remote Sens.* **2023**, *15*, 3099. https://doi.org/10.3390/rs15123099

Academic Editor: Feng Ling

Received: 28 April 2023
Revised: 26 May 2023
Accepted: 7 June 2023
Published: 13 June 2023

Copyright: © 2023 by the authors. Licensee MDPI, Basel, Switzerland. This article is an open access article distributed under the terms and conditions of the Creative Commons Attribution (CC BY) license (https://creativecommons.org/licenses/by/4.0/).

Keywords: ALOS-2 PALSAR-2; SAR; inundation; tropical peatland; remote sensing; meteorology; Congo Basin; radar; wetlands

1. Introduction

Wetlands and floodplains cover ~8% of the Earth's land surface [1,2] and store between 16 and 33% of the world's land carbon [2]. In addition to forming an important ecosystem for biodiversity [3], they play an important role in the global carbon cycle, dominating inter-annual variability in methane sources [4–7], with between 20 and 25% of methane emissions estimated to originate from them [8–10]. Peatlands are a type of carbon-rich, high organic content wetland, formed under anoxic, water-logged conditions due to slow litter decomposition and limits on respiration [11,12].

Greenhouse gas (GHG) fluxes from the peat vary significantly with water table depth. Carbon dioxide emissions increase when the water table is below the peat surface and the peat is exposed to the atmosphere, while increased methane production occurs through methanogenic processes when the water level is close to or rises above the peat surface [5,13]. To understand the influence of hydrology on peatland GHG fluxes, it is important to quantify the spatial and temporal variations in water table levels as accurately as possible. By reducing gaps in our understanding of hydrological processes, we can improve our knowledge of the impacts of hydro-climatic processes [14], leading to better-informed policy-making in relation to land-surface dynamics and climate change. Specifically, improved knowledge of inundation duration and extent will help us to quantify changes in GHG fluxes from the peatland complex under projected climate or land-use change and may also help with the validation of outputs from process-based models [15].

The central Congo Basin experiences significant seasonal and spatial variations in inundation [16]. Frappart et al. [17] has compiled a comprehensive overview of the various methodologies used to assess surface water storage (SWS) anomalies in this region. These methods include interferometric SAR (InSAR) [15,18,19], the use of digital elevation models (DEMs) in conjunction with satellite-derived surface water extent for determining SWS [20,21], employing altimetry-derived water levels combined with satellite-based estimates of water extent [22–24] and using a combination of remotely sensed products to solve the water balance equation, which accounts for rainfall, groundwater input, runoff and evapotranspiration [18,25].

Becker et al. [26] used the Global Inundation Extent from Multi-Satellite (GIEMS) data and ENVISAT altimetry data to estimate water-level maps and SWS across the Congo River Basin (CRB), including the floodplain and wetland regions, for the period 2003 to 2007. They calculated the mean annual variation in the CRB SWS as 81 $\pm$ 24 km^3, which aligns with more recent findings from Kitambo et al. [27], who estimated monthly SWS dynamics over the CRB at 0.25° resolution, for the period 1995 to 2015, using a combination of water level heights from virtual altimeter stations and the water extent from the updated GIEMS-2 dataset [28]. They found strong seasonal and inter-annual variability in the SWS, with the Middle-Congo sub-basin showing the highest variability in the mean amplitude of the SWS volume.

Land-surface modelling techniques have also been used to estimate the CRB surface water extent dynamics; for example, Tshimanga and Hughes [14] applied the Pitman model, a semi-distributed rainfall-runoff model, across the CRB, with the aim of understanding the processes of runoff generation. They were able to simulate the timings and magnitude of water flow maxima and minima; however, the model was not able to generate water level heights.

The Cuvette Centrale is the second largest wetland in the tropics and was recently found to contain the largest region of tropical peatland [11], with an estimated extent of 167,600 km^2, and to store 29.0 Petagrams of carbon (Pg C) (95% CI, 26.3–32.2 Pg C) [29]. It is situated in the central lowland region of the Congo Basin and spans the Republic

of the Congo (RoC) and the Democratic Republic of the Congo (DRC). The two main rivers running through the region are the Congo and the Ubangui, which separate the two countries. Other large rivers within the region are the Sangha and Kasaï [30]. While the peatlands to the east of the Congo River are largely in floodplain locations and receive additional water inputs from riverine flooding and groundwater, those to the west, in the RoC and parts of Northern DRC, are largely located in inter-fluvial basins, and, as they are hydrologically separated from the river system, they receive most of their hydrological input from rainfall [11,25,31], and may, therefore, be more vulnerable to dry periods and climate change impacts.

The studies highlighted so far have improved our understanding of the surface water extent and storage dynamics of the central Congo Basin, but are limited in their usefulness for assessing surface-water dynamics for the non-flood-prone regions of the Cuvette Centrale peatland complex. Altimeters primarily measure water levels over permanent water bodies, including lakes and rivers, and interpolation of these data is, therefore, best suited for flood-prone regions, and would not be representative of ombrotrophic (rainfed) peatland regions. There remains a gap in our knowledge relating to inundation dynamics across the ombrotrophic peatland regions [32,33].

Alternatively, direct in situ water table data may be used, and some are available from water loggers installed in the Cuvette Centrale region [32,33]; however, they are limited in their spatial and temporal coverage. The peatlands are difficult to access to first place water loggers and then to adequately service them, and the logger's lifespan can be short due to the harsh swamp conditions. Additionally, water logger data are at point locations, where the conditions may not be representative of the hydrological dynamics of the surrounding area due to micro-topographical features evident on a spatial scale of metres, which have been shown to result in height variations of $\pm$16 cm to 1 standard deviation in a natural (undrained) tropical peatland in Central Kalimantan, Indonesia [34,35].

To adequately describe peatland inundation at the regional scale necessitates the use of satellite observations covering large spatial extents and available over long time periods. Such data can be validated to some extent using the more limited point coverage of in situ measurements.

Synthetic Aperture Radar (SAR) is an active remote sensing instrument operating at microwave wavelengths. It offers significant advantages for monitoring changes in tropical peatland inundation. SAR's capability to penetrate cloud cover and, at long-band (L-band) wavelength, the tree canopy makes it particularly useful in the context of high humidity conditions and the extensive tree cover prevalent in most tropical peatlands. SAR data can be used to monitor the evolution of flooding across vegetated regions due to increased backscatter, occurring via the double-bounce mechanism [36–38], as the water level increases. Various studies have attempted to map wetland inundation using SAR imagery, particularly L-band SAR in regions of dense forest, including the Japanese Earth Resources Satellite, JERS-1 (available from 1992 to 1998) [39], The Advanced Land Observing Satellite (ALOS) Phased Array L-band Synthetic Aperture Radar (PALSAR) (2006 to 2011) [40] and ALOS-2 PALSAR-2 (2014 to present) [38]. Rosenqvist et al. [39] used two JERS-1 SAR images to investigate the usefulness of radar imagery for characterising seasonal flooding dynamics across the Congo Basin, and found potential for the maximum extents of flooding to be determined, while it was more challenging to determine the dynamics and variability of the flooding due to the complex hydrological mechanisms across the basin. The flood pulse seasonality varies north and south of the equator, making it challenging to identify radar images representative of the minimum and maximum SWS corresponding with the flood evolution dynamics of each [39]. Rosenqvist et al. [38] progressed on their previously developed methods used to map inundation using JERS-1 and ALOS PALSAR by mapping the minimum and maximum extents of inundation across the Amazon basin using a decision tree classification algorithm applied to time series of ALOS-2 PALSAR-2 ScanSAR data. They were successful at capturing the inundation extents, but comparisons with a network of river gauges showed that they were not able to estimate water level,

attributing this in part to the low temporal availability of the SAR data (42-day return cycle). Lee et al. [15] combined the water extent from L-band ALOS PALSAR images with interpolated virtual altimetry station time series and vegetation density data, derived using the Moderate-resolution Imaging Spectroradiometer (MODIS) Vegetation Continuous Field (VCF) instrument, to produce the first high-resolution (100 m) water level maps across the Cuvette Centrale wetlands for selected dates between 2006 and 2008 with ALOS PALSAR scene availability. This enabled improved estimation of the evolution of the region's SWS and better constrained spatially interpolated water level maps.

While previous studies have succeeded at mapping surface water extent and it has been shown that L-band SAR data can be used to map water levels in densely forested regions [15], we lack high spatiotemporal resolution maps of water level variation that can capture inundation dynamics over rainfed regions of the Cuvette Centrale. To address this, we used the high temporal (daily) pattern of net water input (rainfall minus evapotranspiration, not accounting for run-off or groundwater inputs) together with the less frequent but higher spatial resolution (100 m) L-band ALOS-2 PALSAR-2 ScanSAR data, which, at approximately 23.5 cm wavelength, can effectively see through the canopy to the peat surface, to interpolate the SAR imagery to daily resolution. We then used in situ water table depth measurements, recorded during expeditions along multiple transects in the RoC and DRC [29,33], to develop a transfer equation between the SAR backscatter and water level, enabling us to estimate the daily evolution of water level across a sub-region of the Cuvette Centrale. In a rainfed hydrological system, the level of inundation correlates directly with spatial and temporal variations in rainfall, while water level changes in flood-prone regions will decorrelate quickly with the accumulated rainfall input at that location due to the additional time-lag component of water input from upstream rainfall. We use pixel-wise correlation statistics to compare the PALSAR-2 backscatter with the net water input time series. High pixel-wise temporal correlation is indicative of largely rainfed hydrological dynamics, while low or insignificant correlation statistics are indicative of a region receiving additional water input, e.g., from flooding, run-off contributions, or net groundwater output in sloped regions. The three key questions we seek to address within this research are:

1. How does the inundation of tropical peatlands in the Cuvette Centrale vary spatially and temporally?
2. How does water level correlate with net water input across the peatlands, and can this be used to distinguish between areas of the Cuvette Centrale that are largely rainfed and where flood or additional groundwater dynamics play a significant role?
3. What are the differences in peatland hydrological inputs to the east and west of the Congo River?

The use of L-band SAR data to map surface-water dynamics on a high resolution, e.g., a 1-hectare grid, rather than for delineating the extent of flooding, as has been carried out in previous studies, enables more precise mapping of water levels across the peatlands. This is required for bottom-up estimation of GHG emissions from the peatlands. Additionally, high-resolution maps of temporal variations in water level would enable us to make the best use of recently developed land cover maps of the Cuvette Centrale [11,29] to distinguish differences in GHG emissions between the two main peatland vegetation types, palm and hardwood swamp. The Cuvette Centrale peatlands are vulnerable to drying and are on a climatic threshold [41]. Increasing temperatures due to climate change will increase evapotranspiration and may result in a reduction in net water input to the peatlands. A high spatial and temporal resolution water level map at the basin scale could be used to assess the seasonality of inundation and identify which peatland areas are most vulnerable to climate change and becoming a carbon source through increases in carbon dioxide emissions when water levels are low.

The methods we describe here for distinguishing rainfed from flood-prone regions and to temporally interpolate SAR data using the pattern of net water input can usefully be applied to estimate water levels in other vegetated ombrotrophic wetland regions.

2. Methods and Materials

2.1. Study Area

We focused our study on a subset region of the Cuvette Centrale (Figure 1), corresponding with the 350 × 350 km area of the PALSAR-2 imagery we used. The locations where water table depths were measured are highlighted on the map.

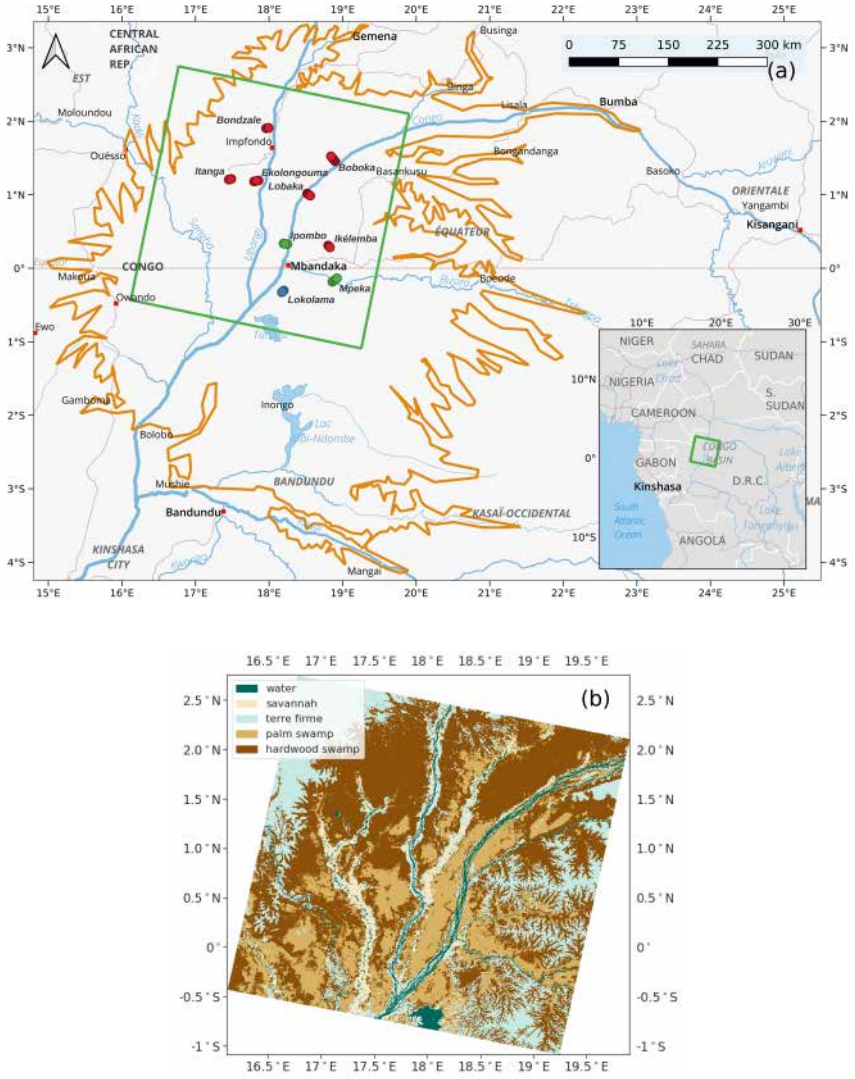

Figure 1. (**a**) The green border shows the extent of our study area within the Cuvette Centrale region, corresponding with the extent of the time series of PALSAR-2 scenes we used. The orange outline is the footprint of the peatland complex, derived from Crezee et al. [29]. Highlighted are the transects where water table depth measurements were taken during either the dry (red), wet (blue) or both dry and wet (green) seasons [33]. Additionally, two water loggers are located in the Ekolongouma region and three are in the Lokolama region. The inset map shows where our study area is located in Central Africa. (**b**) Land cover corresponding with the study area, derived from Crezee et al. [29].

Figure A2 provides further information about the terrain characteristics of this region. The peatland elevations vary from ∼300 to 340 m above sea level (Figure A2a). The terrain slope characteristics are distinct between the peatlands to the west and east of the Congo River, with fluvial-connected peatlands located in the eastern DRC region, while the peatlands lie mainly in inter-fluvial basins to the west of the Congo River (Figure A2c).

2.2. Data

2.2.1. SAR Data

The ALOS-2 satellite mission was launched in 2014 by the Japan Aerospace Exploration Agency (JAXA), with the Phased Array L-band SAR 2 (PALSAR-2) instrument on board. One of its main objectives was to monitor environmental changes globally, including the inundation dynamics of wetland regions [42]. We used 17 dual-polarisation PALSAR-2 scenes obtained through the JAXA G-Portal interface (https://gportal.jaxa.jp/gpr/?lang=en, last accessed: 13 April 2023) in CEOS format at the level 1.5 geo-referenced stage of processing. These data include a basic radiometric correction but not speckle reduction, terrain correction, or geo-referencing. The polarisations they include are the Horizontally-transmitted, Horizontally-received (HH) and Horizontally-transmitted, Vertically-received (HV) amplitude and intensity bands. Yuan et al. [43] used the ALOS PALSAR HH polarisation together with altimetry data to map water level changes over Île Mbamou in the Congo Basin, due to its higher sensitivity to water level [40]. The HV polarisation is more sensitive to vegetation characteristics, and the ratio of the two (HH:HV) has previously been used to improve identification between flooded and non-flooded pixels when using Sentinel-1 SAR data at C-band resolution [44].

All images obtained were taken in the descending orbit direction. The time series of 17 collocated SAR images we use includes a set of 15 subsequent scenes from 2019 to 2020, each separated by 42 days in most cases and 28 days in two cases, and a second set of two subsequent scenes from 2021. There is a gap of ∼11 months between the end date of the first set and the start date of the second. Our final spatiotemporal water depth maps are produced for dates that fall within the start and end dates of each of these two sets.

2.2.2. Meteorological Data

Rainfall is highly variable across the Cuvette Centrale both spatially and temporally, and our study requires sufficiently high-resolution data to assess how rainfall variations relate to temporal changes in backscatter in the PALSAR-2 imagery. We use the daily Climate Hazards Center Infrared Precipitation with Stations version 2 (CHIRPS-2) rainfall dataset [45], available at 0.05° resolution (5.55 km resolution at the equator). An intercomparison study of remotely sensed rainfall products showed it to be the highest resolution product available that was effective at reproducing the spatial variability of Central African rainfall and performed well on the inter-annual scale [46]. Additionally, Santos et al. [47] highlighted the benefits of using CHIRPS-2 rainfall data within the Soil and Water Assessment Tool (SWAT) model over the Congo Basin, in comparison to other satellite-derived rainfall data.

Potential evapotranspiration (PET) is the maximum amount of water that could potentially be evaporated from an area given sufficient water availability, while actual evapotranspiration (AET) is the amount of water evaporated, limited by water availability. In swamp regions, where there is sufficient water availability either above or below the surface, changes in the AET are controlled mainly by temperature and humidity variations, and the AET is equal to the PET [48]. We use daily PET data from the National Oceanic and Atmospheric Administration (NOAA), available at 1° spatial resolution from the USGS FEWS Net platform (https://earlywarning.usgs.gov/fews/product/81, last accessed: 18 April 2023) and MODIS SSEBop AET data at 1 km spatial and dekadal (10-days) temporal resolution, also available from the FEWSNet platform (https://earlywarning.usgs.gov/fews/product/461, last accessed: 18 April 2023).

2.2.3. In Situ Data

We used water table depth measurements taken at 250 m intervals along transects, collected during multiple field sampling trips [29] (see Figure 1), to arrive at a transfer function between the SAR backscatter and water level that we can then apply across the full extent of the imagery. Further details about the transect sampling dates are included in

Table A1, and details about the field campaigns are provided by Crezee et al. [29] and in the PhD thesis by Crezee [33].

Additionally, we used measurements from five in situ automated water table loggers [29,32] to assess the spatial correlation between the derived water level patterns and long-term time series of water levels at specific sites (see Table A2 for further details of their locations and date ranges). Two are located in the Ekolongouma region of the RoC (Figure 1) and log the water table depth at 10-min intervals, while three are located in the Lokolama region of the DRC and log the water table depth at 20-min intervals. These data have been corrected using local air pressure measurements from nearby barometric loggers.

2.2.4. Altimetry-Derived Surface Water Level

Satellite radar altimetry can estimate water levels by measuring the time it takes for a microwave pulse to be backscattered from water and returned to the sensor. Currently, radar altimetry processing is applied across selected permanent water body locations to produce virtual station time series of water levels. Automation of the process requires identification of where the altimeter crosses water bodies and, therefore, the easily identifiable rivers, lakes, and reservoirs are most often used, rather than tropical peatland regions with their variable surface-water dynamics [49]. We used four altimetry time series, collocated with regions of peat swamp within our study area, to validate the derived daily water-level data: two from the Sentinel-3A radar altimeter (27-day resolution), and two from the Jason-3 radar altimeter (10-day resolution). The data were downloaded from the Hydroweb site (https://hydroweb.theia-land.fr/, last accessed: 7 March 2023). Kitambo et al. [50] provide a more detailed description of the analysis of altimetry virtual stations over the Congo Basin.

2.2.5. Land Cover and Terrain Data

We used an approximately 50 m resolution land cover map of the Cuvette Centrale region, developed by Crezee et al. [29], to mask our data for permanent water bodies and non-peatland land class areas. Crezee et al. [29] included ALOS PALSAR yearly mosaic HH polarisation data in their land cover map model but found that it did not distinguish between peat swamp vegetation classes. We, therefore, use ALOS-2 PALSAR-2 HH data to explore the differences in derived water levels between the two dominant peatland vegetation classes identified by Dargie et al. [11] and Crezee et al. [29]: palm and hardwood swamp.

In our discussion of the results, we refer to terrain data, including the MERIT Hydro Digital Elevation Model (DEM) and Height Above Nearest Drainage basin (HAND) datasets [51] at 90 m resolution, retrieved from Google Earth Engine; the slope of the terrain, which we derived from the MERIT DEM using GDAL tools and the Relative Topographic Position Index (RTPI) which we calculated from the DEM using the Whitebox tools Python package. The MERIT DEM corrects for tree height bias, which results in terrain slope distortion, significantly affecting low-lying tropical swamp regions, including the Congo Basin [51].

2.3. Methods

In this section we describe our use of the PALSAR-2 data; the derivation of the net water input data from rainfall, potential evapotranspiration (PET) and actual evapotranspiration (AET) data; the combined use of these data to interpolate the PALSAR-2 image stack to daily resolution; the use of a transfer function and pixel-wise correlation statistics to derive the final modelled time-series of water-level evolution across peatland regions and validation of these data.

2.3.1. PALSAR-2 Data

For the purpose of inundation mapping, we rely on the double-bounce mechanism [36–38], which happens when the radar signal undergoes specular reflection from a smooth surface

(e.g., water) and then encounters a vertical surface (e.g., a tree trunk) from which it is backscattered to the sensor in the same direction as the incident signal, enhancing the signal return from that location (Figure 2). Where this happens, locations appear brighter in the imagery, enabling estimation of inundation, by defining relationships between surface-water level and radar backscatter.

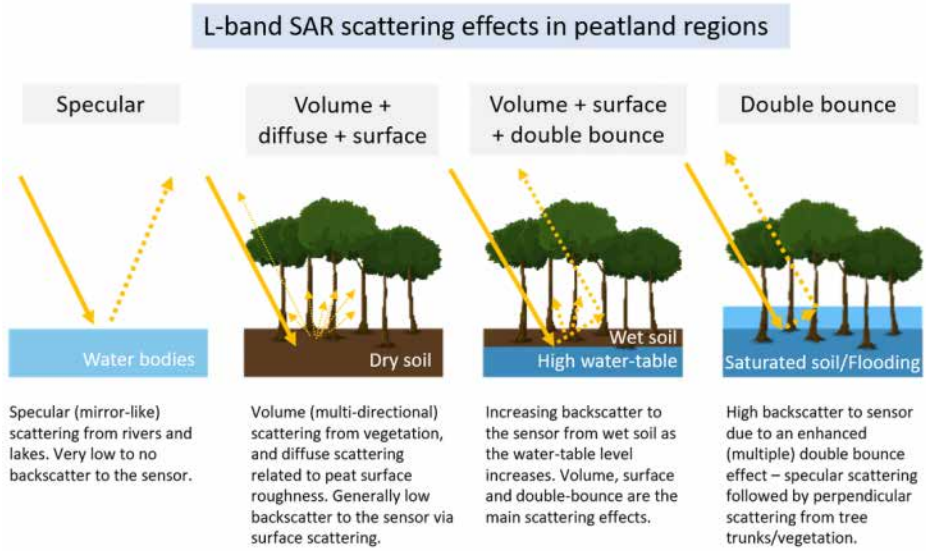

Figure 2. Summary of the backscattering mechanisms involved between L-band SAR data and regions of tropical peatland.

The pre-processing stages for creating level 1.5 PALSAR-2 data included range compression, multi-look azimuth compression and applying radiometric and geometric corrections. We applied additional post-processing steps as detailed in Figure 3. A more detailed description of these steps is included in Appendix A.1.

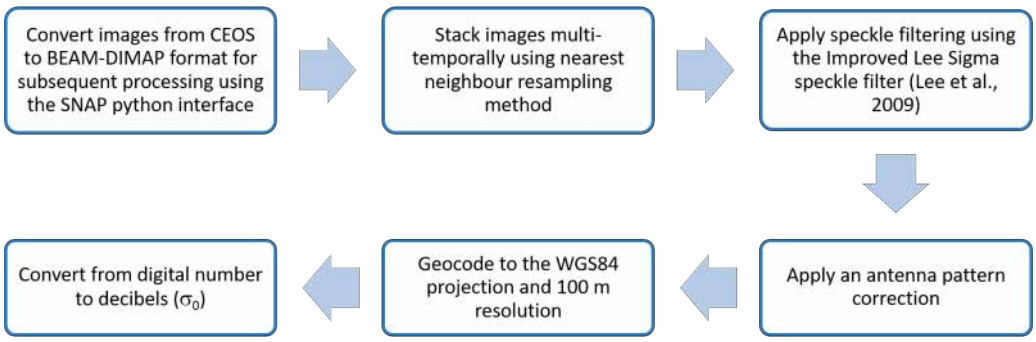

Figure 3. A summary of the post-processing steps applied to the ALOS-2 PALSAR-2 time series of images [52].

2.3.2. Calculation of Daily Net Water Input

We re-gridded the 0.05° CHIRPS to the same resolution as the AET data (0.01°) using a bilinear interpolation. This was carried out only for the purpose of the data grids being co-located, rather than to enhance the resolution of the rainfall data.

To approximate the daily AET, we applied the temporal pattern of the daily PET data to the dekadal (10-day) AET data. This involved summing the daily PET over the same dekadal periods as the AET data and calculating daily weightings, corresponding with the

distribution of the daily PET over this period. We then applied these daily weightings to the dekadal AET to estimate daily AET. This method effectively applied a pixel-by-pixel multiplying factor to the daily PET to calculate the daily AET from the pattern of the PET. In doing this, we made the assumption that the AET is approximately equal to the PET in wetland regions, as there is always water available to be evaporated.

The Cuvette Centrale region experiences two dry seasons: December, January, and February (DJF) and June, July, and August (JJA), and two wet seasons: March, April, and May (MAM) and September, October, and November (SON). To validate our assumption that AET approximately equals PET within our study region, we first summed the PET over the same dekadal periods as the AET, and then summed their differences over the three-month dry and wet seasonal periods, to arrive at the total seasonal differences between the AET and PET at each pixel. The daily net water input at each pixel was then calculated as the difference between the daily rainfall and the derived daily AET estimate. It is important to note that this method provides net water input estimations with the highest accuracy for directly rainfed peatlands that do not experience significant additional surface or sub-surface runoff contributions.

2.3.3. Determining Which Areas Are Rainfed

We calculated pixel-wise temporal correlations between the change in backscatter between pairs of subsequent images in the PALSAR-2 HH time series stack (δHH) and the time series of the corresponding accumulated net water input between each pair of subsequent images. We used the resulting pixel-wise correlation statistics, including the correlation, slope, p-value and standard error, to determine the extent to which each pixel can be classed as rainfed, receiving its water inputs from direct rainfall.

We also calculated the number of days of net water accumulation that results in the highest correlation between these two datasets, allowing us to map more clearly the extent to which different areas are directly rainfed, receive additional surface or sub-surface hydrological input or are flood-prone.

2.3.4. Mitigating for Terrain Variability When Estimating Pixel Water Level

As a result of spatial variations in the gradient of the pixel-wise correlation, we decided that the interpolation to daily values of SAR data using the pattern of the rainfall data should be applied using the best-fit pixel-wise correlation pattern for each individual pixel. This means that any differences in backscatter due to differences in terrain, e.g., slope, aspect, tree density or dominant vegetation type within a 1 ha pixel, can be accounted for to some extent. As such, we were then able to apply a single linear regression equation across the full image stack extent to transfer the derived daily HH backscatter time series to a water level estimate.

2.3.5. Estimating the Daily Water Level

We describe here the processing steps involved in our use of the PALSAR-2 time series to calculate the evolution of the water table level at 100 m spatial-temporal and daily temporal resolution.

Permanent water bodies have low SAR backscatter values, as the signal experiences specular reflection from their surface, given that there is no vegetation with which it can interact (Figure 2). By looking at the backscatter distribution across the images, we identified permanent water bodies as pixels with a maximum time-series backscatter value below −11 dB, which is in agreement with the value found by Kim et al. [53]. Using the maximum value across the time series, rather than a single image, ensures that any areas where the vegetation may sometimes be inundated to the point where the water level is above the vegetation, are not falsely classified as permanent water bodies. Within the Cuvette Centrale region, this is unlikely to occur as the water levels are not that high, with a variation in river height of 1.5 to 4.5 m [50]; however, it would become important if the

methods described here were to be extended to other wetland regions, e.g., the Pastaza Marañon Foreland Basin (PMFB) in Peru where higher levels of inundation are experienced.

To interpolate the HH SAR time series from between 28 and 42 days to daily resolution, using the pattern of the daily net water, we calculated the forward and backward evolution of HH backscatter from the previous and next images in the stack, respectively.

We used the forward equation:

$$HH_n = HH_{i0} + \frac{\sum_{d=0}^{n-1} NW_{daily}}{m} \quad (1)$$

and the backward equation:

$$HH_n = HH_{i1} - \frac{\sum_{d=n}^{i1-1} NW_{daily}}{m} \quad (2)$$

where HH_n is the daily HH backscatter value to be calculated; i_0 is the start image and i_1 is the end image for each pair of subsequent images in the original HH stack; m is the gradient of the pixel-wise correlation between the δHH and δNW time-series (unique on a pixel-by-pixel basis) and NW_{daily} is the daily net water input.

We also investigated implementing the daily HH interpolation using two methods: (1) only the forward equation described above and (2) a combination of the forward and backward equations, each calculated to the mid-point between subsequent images, such that every interpolated value is based on the closest image. However, although the range of HH daily values was within the expected range in both cases, there were noticeable steps in the values between the last and second-to-last days when using the forward-interpolation only, and between the mid-interpolation dates when using both the forward and backward interpolations. This occurred to a greater extent for pixels with a lower correlation between the HH backscatter and the daily net water input. These locations are not fully rainfed and the local slope could lead to water in/out flow, or there may be some flooding potential in riverine areas. To mitigate this, we applied logistic growth and decay functions to the forward and backward equation interpolated outputs. This resulted in a 50% influence on the central interpolated date's image values from each of the previous and following HH backscatter images and an exponentially increasing contribution from the closest image date as the interpolation tends towards it. The logistic decay function is calculated as follows:

$$f(x) = \frac{1}{1 + e^{10(x-0.5)}} \quad (3)$$

and the growth function:

$$f(x) = \frac{1}{1 + e^{-10(x-0.5)}} \quad (4)$$

where x is the number of days between subsequent PALSAR-2 scenes. The value of -0.5 is used to centre the function's mid-point so that it lies halfway between subsequent scenes and a scaling factor of 10 is used. These functions are shown graphically in Figure A1.

Additionally, we calculated a daily linear interpolation between subsequent image dates. These data were used to gap-fill the final HH backscatter interpolation in regions prone to flooding or where the rainfed contribution of a pixel's total water input is low due to surface or sub-surface run-off/run-in.

We performed a linear regression analysis between the water table depth measurements along the transect (Figure 1) and the PALSAR-2 HH backscatter data. Subsequently, we applied this derived transfer equation to the interpolated daily time series of HH backscatter, enabling us to determine the spatial and temporal variations in the water levels.

We used pixel-wise correlation statistics to identify rainfed areas as being located where there are significant correlations between the net water accumulations and the

HH time series. For these regions, we used the pattern of daily net water accumulations between subsequent image dates to model variations in the water table level. For all other regions, where changes in water level do not correspond well with the net water input (accounting for rainfall and evapotranspiration alone), we applied a linear interpolation between image dates.

2.3.6. Determining Water Level Variability

To assess the spatial and temporal variability of the derived daily water level time series, we calculated five metrics across peatland pixels within the study area for both individual months and the full 20-month period: (1) the minimum and (2) maximum water levels for each pixel, (3) the corresponding amplitude (maximum−minimum), (4) the mean water level and (5) its standard deviation. Additionally, we calculated the percentage of days that the water level was at or above the peat surface across the full 20-month time series.

These metrics helped us to identify where the largest fluctuations in water level are experienced; which areas of the peatlands are seasonally inundated and, therefore, might be more susceptible to drying under future climate change scenarios and the differences in variability between largely rainfed regions and those that receive additional water input from riverine flooding or runoff.

To explore the relationship between water level and swamp vegetation type, we ran a one-way ANOVA test between the categorical variable, peat swamp type (hardwood and palm swamp) and the standard deviation, minimum, maximum and mean values of the water level. We used the outputs of the ANOVA tests to calculate the Eta squared (η^2) values. η^2 has parallels with the R^2 value in that it measures the degree to which the variance in the categorical variable is related to the variance in the continuous variable. We also calculated the mean value of each of the water level variability metrics for palm and hardwood swamp types. Additionally, we calculated the mean values for each of these metrics across all time steps for hardwood and palm swamp pixels respectively.

2.3.7. Validation of Modelled Water Levels

To validate the modelled daily water level maps, we assessed the correlation between the patterns of the modelled and measured water level data using time series of in situ water level logger data, available at five locations within our study area. These water logger data were held aside specifically for validation purposes. The peatland micro-topography can be highly variable and is characterised by raised hummocks and depressed hollows that become inundated first [34]. It is not known if the water logger placements were representative of the average elevation and, therefore, the average water level conditions across the 1 ha area they lay within, corresponding with the SAR pixel from which we retrieved the backscatter values. We were therefore more interested in the direction and rate of change between the time-series patterns than the absolute values. We calculated correlative statistics, including the non-parametric Pearson's R (and R^2), Kendall's τ and Spearman's ρ, to compare these two-time series. Pearson's R and Spearman's ρ provide measures of the strength of the relationship between two variables. R measures the linear correlation and R^2 is a measure of the percentage of variability in the first (independent) variable that can be explained by the second (dependent) variable, while ρ measures the rank correlation, which disregards the order of the original data and is useful where the rate of change in the relationship between two variables is not constant. This can be the case when comparing modelled (large spatial area) and water logger (point location) data, where the rate of change in water level may not be representative between the two spatial scales. Kendall's τ additionally provides a measure of how correlated the directions of the relationship between two variables are. In our case, this would be a measure of whether the water logger and modelled data are in agreement about whether the water level is rising or not.

We also normalised the altimetry and modelled water level data and compared their patterns, as we did with the water logger data. We used the patterns, rather than the absolute values, for three reasons: the altimetry data is referenced to the geoid (height above sea level); the altimeters measure at C-band and can have large uncertainties in estimated water level heights, especially over wetlands where there is dense vegetation and increased signal attenuation and the altimeter virtual stations are likely located over stream areas that traverse the 1 ha pixel area, such that the altimeter-measured variations in water level may be greater than those over the neighbouring swamp vegetation due to the flood protection provided by levees.

2.4. Use of Elevation Data in the Discussion of the Results

The relative topographic position index (RTPI) is a measure of the difference in elevation between a pixel and the mean elevation of its surrounding pixels within a defined filter box extent [54]. We derived the RTPI from the 90 m MERIT DEM using the Whitebox Tools Python package RTPI function, with a 56 by 56 (approximately 5 × 5 km) filter kernel.

3. Results

3.1. Validation of the Combined Use of Actual- and Potential-Evapotranspiration

We confirmed that our assumption, that AET approximates PET in wetland regions, is a valid one across our study area. The total seasonal differences between the dekadal AET and PET are shown in Figure 4 for the peatland region within the ALOS image stack extent. These were small compared to the corresponding total evapotranspiration, with a mean summed difference of 10.9 mm over the three-month seasonal periods (Figure 4b). In some areas of the Cuvette Centrale, flooding continues or increases into the dry seasons (December to February and June to July) due to the time lag in local river level increases resulting from upstream hydrological inputs [50].

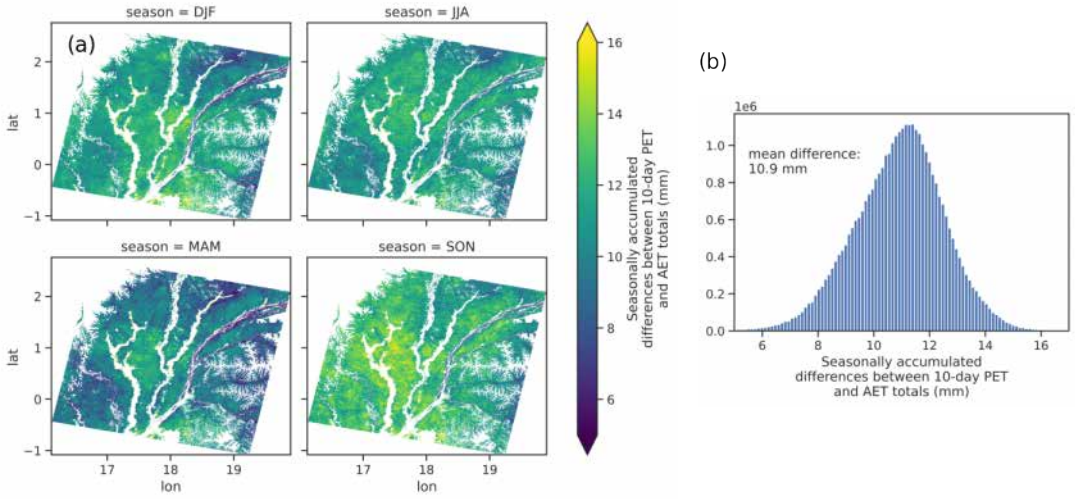

Figure 4. (**a**) The seasonally summed differences in accumulated 10-day Potential Evapotranspiration (PET) and Actual Evapotranspiration (AET) over the study area for the two dry seasons: December, January, February (DJF) and June, July, August (JJA), and two wet seasons: March, April, May (MAM) and September, October, November (SON). (**b**) A histogram showing the full spread of differences between the 10-day PET and AET accumulations.

3.2. The Applicability of the Derived SAR Metrics for Flood Mapping

Over peatland areas, we observed the highest inter-season variability in backscatter in the HH image stack (Figure 5). We tested the use of both the HH and HH:HV image stacks and we found that the HH data alone was the most useful for understanding the evolution of water level over our study area, as the division by HV resulted in the

dampening of the time-series variation and a reduced ability to identify changes in water level under the canopy. Additionally, the mean pixel backscatter values for peatland regions, calculated temporally across the image stack, are lower for the HV polarisation (−15.5 to −10.5 dB) than for the HH polarisation (−3.5 to −8 dB). There is a striping effect in the original PALSAR-2 data corresponding with the instrument scan lines. These stripes are barely noticeable for individual scenes, as the change in backscatter due to them is very low, and their impact is minimal in comparison to the collocated features that represent changes in water level/vegetation conditions. However, due to the lower HV polarisation backscatter signal, the cumulative impact of the striping effect is more apparent when calculating statistics across the image stack. We, therefore, progressed with our study using the HH image stack.

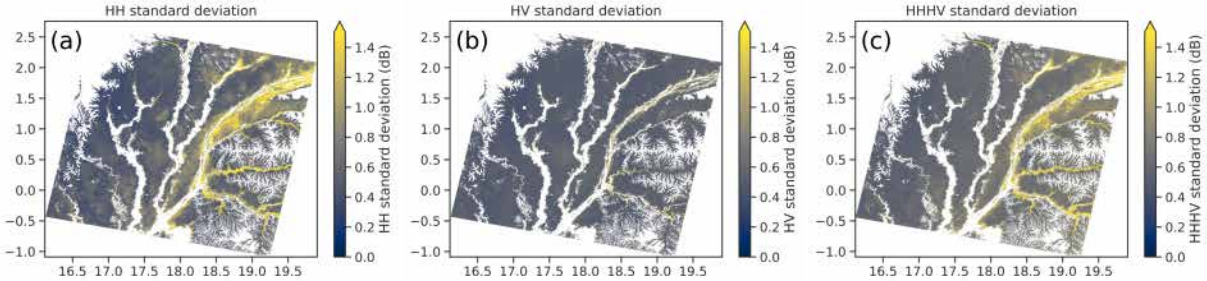

Figure 5. The standard deviation, across all image stack time steps for ALOS-2 PALSAR-2 polarisation: (**a**) HH, (**b**) HV and (**c**) HH:HV. Only peatland pixels are included.

3.3. Identification of Rainfed Regions

We distinguished rainfed and flood-prone regions using pixel-wise correlation statistics between the SAR backscatter and net water input time series. These classifications determined our use of the net water input interpolation model for rainfed pixels (see Methods Section 2.3.5) and a linear interpolation model between the SAR backscatter values for flood-prone regions. In this section, we summarise our classification of rainfed versus flood-prone areas; the period over which the pixel HH backscatter and, therefore, the water level, remains correlated with the net water input and spatial variations in the pixel-wise correlation statistics.

3.3.1. Pixel-Wise Correlations—Statistical Summary

Table 1 provides summary statistics of the pixel-wise correlations and Figure 6 shows the corresponding mapped pixel-wise correlation, *p*-values, gradients and standard errors.

The pixel-wise correlation statistics (Figure 6) provide an indication of the degree to which locations are rainfed or influenced by additional flood inputs in riverine locations. These were calculated between the changes in SAR backscatter and net water accumulations over the 42-day intervening period between available PALSAR-2 scenes and, therefore, cannot capture where there may be significant correlations that persist over shorter periods of time, as there will likely be decorrelation as this period progresses for locations which are not directly, or only partially, rainfed (e.g., the cumulative impacts of additional hydrological inputs or outputs from groundwater due to pixels being located in sloped regions, or prone to flooding at certain times of the year). For locations with a pixel-wise correlation p-value < 0.15, the average length of time over which the SAR backscatter remains correlated with the net water input is 20 days. Since our model interpolates the SAR backscatter using the pattern of net water accumulation to/from the nearest image date, at a maximum interval of 21 days, we used a threshold p-value of 0.15 to delineate the locations where the rainfed model could be applied and where the linear model should alternatively be used. The mean standard error in water level of the pixel-wise regressions for these pixels is 3.2 cm (Table 1).

Table 1. Pixel-wise correlation summary statistics using different thresholds of *p*-values associated with the correlation between the net water input and the change in SAR backscatter between successive PALSAR-2 scenes. The column entries show the mean values across all peatland pixels within the study area that meet each *p*-value threshold.

p-Value Threshold	% of Total Study Area Pixels	R^2	Average Value for Maximum Length of Correlation (Days)	Gradient of Pixel-Wise Correlation (cm/dB)	Standard Error (cm)
<0.001	6	0.65	29	11.52	2.43
<0.01	24	0.5	25	9.87	2.8
<0.05	50	0.38	22	8.42	3.04
<0.1	64	0.33	21	7.75	3.12
<0.15	73	0.3	20	7.35	3.17
≥0.15	27	0.01	12	1.34	3.48

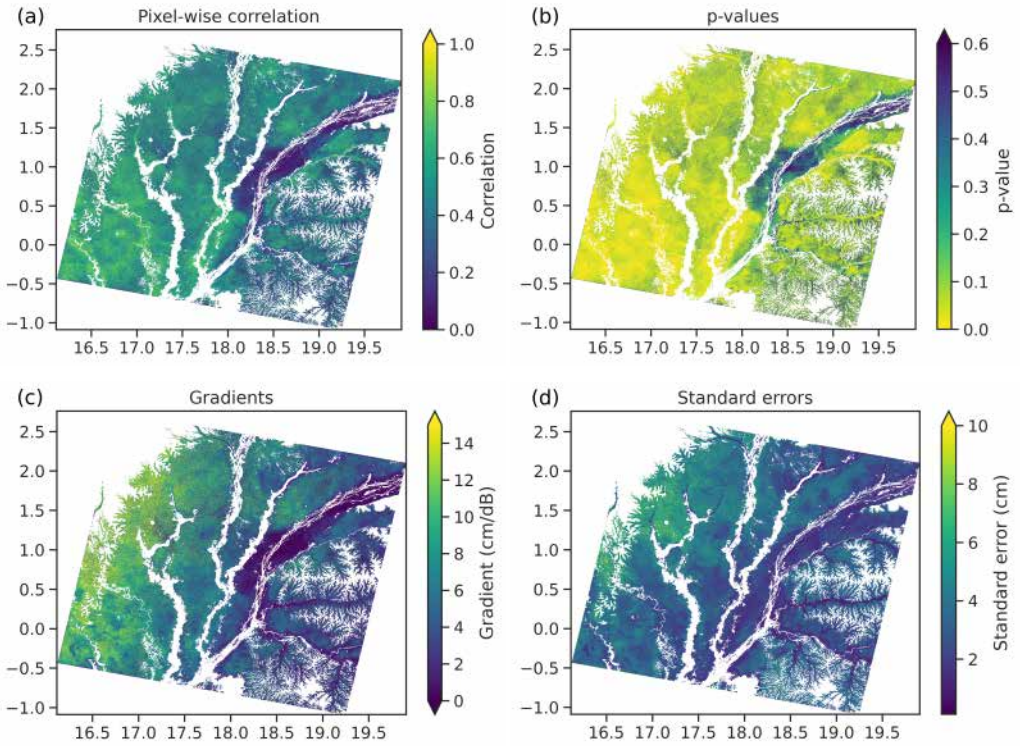

Figure 6. Pixel-wise correlations calculated between time series of the change in SAR backscatter between subsequent PALSAR-2 scenes, δHH, and the corresponding net water accumulations across the ALOS-2 PALSAR-2 HH backscatter stack. (**a**) Correlations, (**b**) *p*-values, (**c**) gradients and (**d**) standard errors of the pixel-wise correlation. Permanent water bodies and non-peatland land cover have been masked.

While all areas receive some direct input from rainfall, the pixel-wise correlations indicate whether a significant portion of the variation in water level can be explained by direct rainfall input. The pixel-wise correlations were applied across the full time-series of the PALSAR-2 imagery, including across all seasons. As a result, some pixels may be classed as rainfed for part or most of the year, while receiving additional groundwater or flood inputs during the wettest times. Our use of a threshold *p*-value < 0.15 (corresponding with an R^2-value > 0.3) allowed for the inclusion of areas that are largely, but not necessarily fully rainfed. Overall, 72.5% of all pixels had pixel-wise correlation *p*-values < 0.15, 64.2% with <0.1, and 50% with <0.05, so we conclude that 72.5% of the peatlands are rainfed to an extent.

Due to the high pixel density (1 ha resolution) of the pixel-wise correlation maps (Figure 6), it can be difficult to draw conclusions visually without zooming in to a much

higher resolution. To address this, we compared the locations of the pixels with the 10% highest and 10% lowest pixel-wise correlations (Figure 7). This distinguishes more clearly peatland locations where the water level is strongly related to the net water input, which lie largely to the west of the Congo River and, especially, to the southwest of the study area (Figure 7a). We also observe negative correlations in some of the floodplain peatlands bordering the Congo River. We determine that the RoC peatlands within our study area (a subset of the Cuvette Centrale peatland complex) are largely rainfed (Figure 6), while riverine locations in the DRC have no direct correlation with rainfall input and are flood-prone, with their water levels correlating more with the hydrological dynamics of the river system.

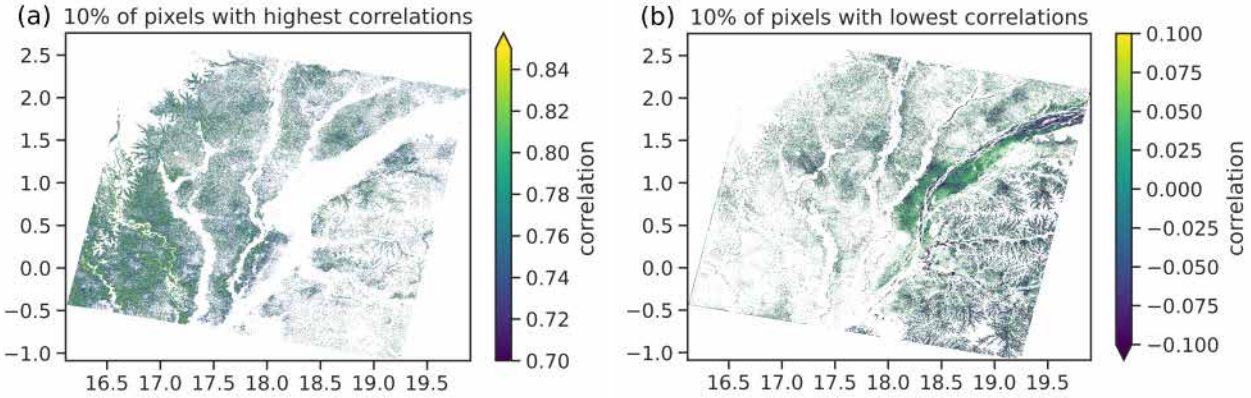

Figure 7. Maps showing the peatland pixels within the study area with (**a**) the highest 10% of pixel-wise correlations and (**b**) the lowest 10% of pixel-wise correlations.

3.3.2. Assessing the Maximum Period of Correlation between SAR Backscatter and Net Water Input

We further identified the degree to which areas are directly rainfed or receive additional flood or surface/sub-surface water inputs using our calculation of the maximum number of days that the HH backscatter remains correlated with the prior accumulated net water input. Figure 8 shows the period of maximum correlation between the HH backscatter and net water input time series. The areas with the highest maximum time of correlation are most likely directly rainfed as the temporal pattern of backscatter does not diverge from the net water accumulation as quickly.

Most images within the stack had 42 days between them (2 with a 28-day gap) and for any date within the daily HH interpolation, there was at most a 21-day time step to the closest image. Generally, the areas with the highest overall pixel-wise correlation (Figure 6a) and lowest corresponding *p*-values (Figure 6c) have a longer period of correlation with net water input (Figure 8). The correlation time between net water accumulation and SAR backscatter varies directly with the correlation between net water accumulation and water-level changes. We observe that inter-fluvial locations in the RoC, to the west of the Ubangui River, and regions of the DRC that are bounded between the Ubangui and Congo rivers have longer periods of continued correlation between net water accumulation and water level.

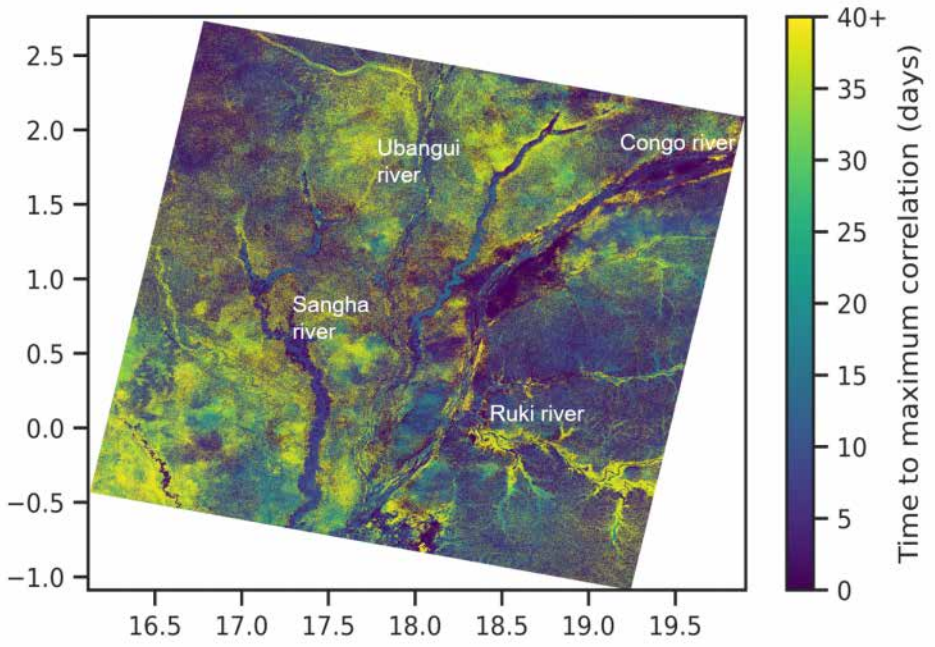

Figure 8. The period of maximum correlation across the extent of the study area—the number of days of net water accumulation that result in the maximum correlation between the ALOS-2 PALSAR-2 HH backscatter and the net water time-series data.

3.3.3. Variability in the Pixel-Wise Correlation Gradient

There is large variability in the gradient associated with the pixel-wise correlation across the peatland area (Figure 6c). The gradient of the pixel-wise correlation is a measure of the quantity of net water input that results in a 1 dB change in the HH backscatter. The lowest gradients are found in floodplain areas, which receive additional water from the river system, while the highest are found in hilly regions that lose some of their water input from rainfall through net run-off (Figure 6c). We also observe that the rainfed, inter-fluvial areas of the RoC have lower pixel-wise gradients at the central points between the rivers that do not flood. This is indicative of water pooling due to the slight terrain slope in these areas (Figure A2c). Over the period of the SAR image stack, the mean value of the gradient was 7.35 cm/dB and the p-value is less than 0.15.

3.4. Transfer Equation between HH Backscatter and Water Level

We arrived at a transfer function between the HH backscatter and water level by calculating a linear regression (Figure 9) between the median transect water depth and the HH backscatter, using data from multiple transect locations (see Figure 1):

$$WTD = 7.45\sigma_0 + 53.2, \quad (5)$$

where WTD is the water table depth and σ_0 is the HH backscatter. Only transect pixels with a minimum water level of 15 cm below the peat surface were included in the final linear regression, as we found that the HH backscatter cannot clearly resolve differences in water level below this depth.

It is interesting to note that the slope of this best-fit relationship, 7.45 cm water level rise/dB, nearly matches the mean gradient over rainfed pixels that we calculated earlier of 7.35 cm net water input/dB. This may indicate that pixels with this value of gradient associated with the pixel-wise correlation are representative of locations where, on average across time steps, the net water input largely translates into water level rises at that particular point without the need to account for additional inputs or outputs from flooding, groundwater or runoff.

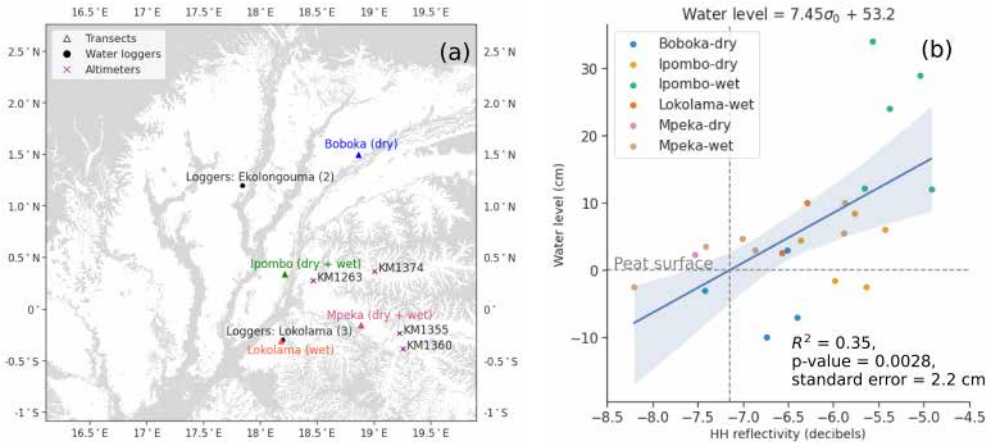

Figure 9. (**a**) Locations of the peatland transects we used within our regression analysis, with water levels above 15 cm below the peat surface. Here, only one marker for each transect is shown for readability and the full transects are shown in Figure 1a. Also shown are the water logger and virtual altimetry station locations. (**b**) A linear regression calculated between the HH backscatter (σ_0) and the median water level depth recorded at each transect location. The dry and wet labels correspond with the seasons during which the measurements were taken, defined in terms of climatological rainfall variability. Further information is provided in Table A1.

3.5. Variability in Derived Water Levels

We applied the transfer equation to the HH backscatter to calculate the daily water level at 1 ha pixel resolution. Figures 10 and 11 show the derived water level summary metrics over our 20-month study period. Figure 10a shows the water level amplitude, calculated as the difference between the minimum and maximum water levels over the study period on a pixel-by-pixel basis (Figure 11a,b). Figure 11c,d shows the mean and standard deviation of the water level variations at 1 ha pixel resolution. We identify the maximum variations in water level in the flood-prone riverine locations to the east of the Congo River, along the edges of the smaller tributary rivers in the DRC (e.g., the Ruki), and in the Southern inter-fluvial region between the Ubangui and Congo rivers. Across the study area, the average pixel water level varies by between 5 and 70 cm, with a mean value of 22.8 $\pm$ 10.1 cm to 1 standard deviation (Figure 10b). Broadly, in the DRC, the highest water level amplitudes are in flood-prone regions, while, in the RoC, they are found in inter-fluvial rainfed regions. There is some localised inundation on the <1 ha scale with higher water level amplitudes due to terrain variability and micro-topographical effects where there are hollows and hummocks.

The corresponding monthly mean, minimum, maximum and amplitude water level variation plots for the full 20-month study period can be found in Appendix B.4, Figures A3–A6. During this period, December 2019 was the wettest month and experienced the maximum water levels (see Figure A5), the maximum range of water levels (Figure A6) and the maximum extent of flooding around the Congo mainstem.

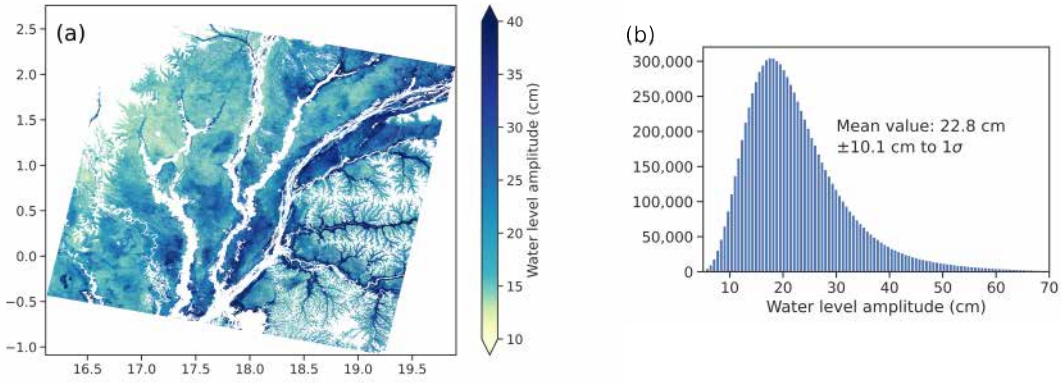

Figure 10. (**a**) The amplitude of the water level across the study area and over the 20-month period March 2019 to October 2020 and (**b**) the corresponding histogram showing the full variability in the amplitude of water levels across all the 1 ha pixels.

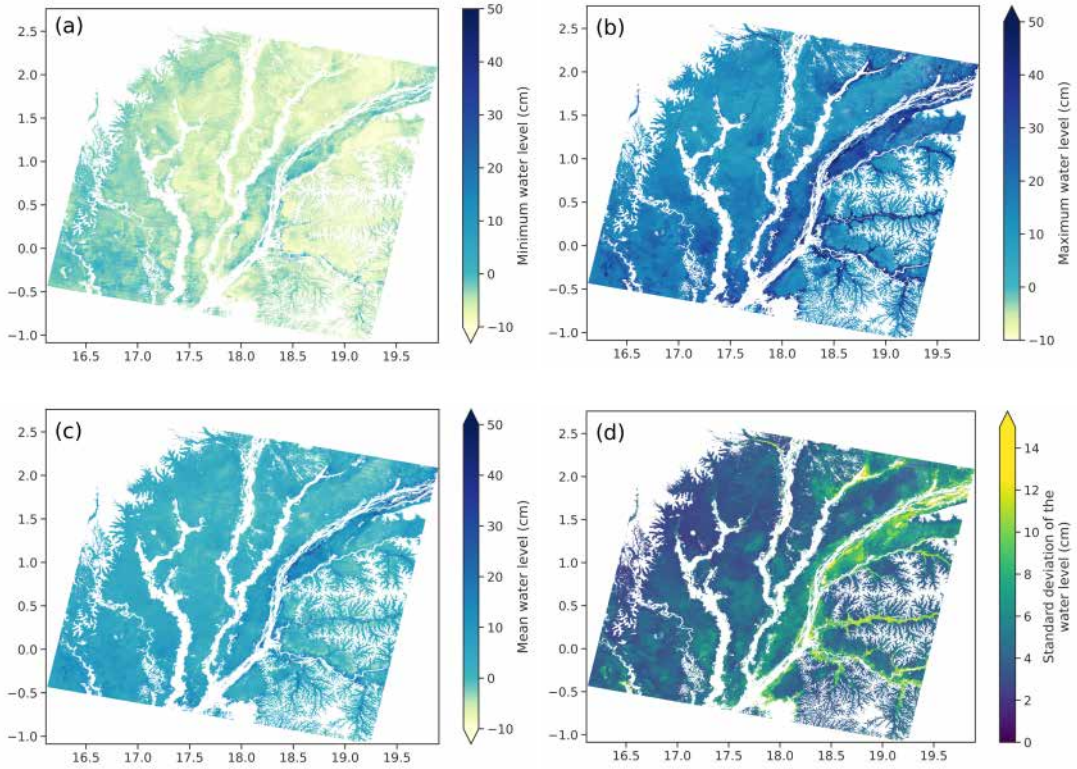

Figure 11. A summary of the variations in water level over the 20-month period from March 2019 to October 2020. (**a**) Minimum, (**b**) maximum, (**c**) mean and (**d**) standard deviation of the water level.

Figure 12 shows the percentage of days during our study period when the water level was above the peat surface. This is an important metric, as it gives us an indication of the amount of time the water level was sufficiently high for the process of methanogenesis to occur and for the net flux of methane from the peatlands to the atmosphere to be positive. There are some regions of peatland that were permanently inundated during this period, including (1) the floodplain regions to the east of the Congo River and between the Ubangui and Congo rivers; (2) rainfed regions in the inter-fluvial basins; (3) the southwest rainfed region of the study area (see Figure 12b).

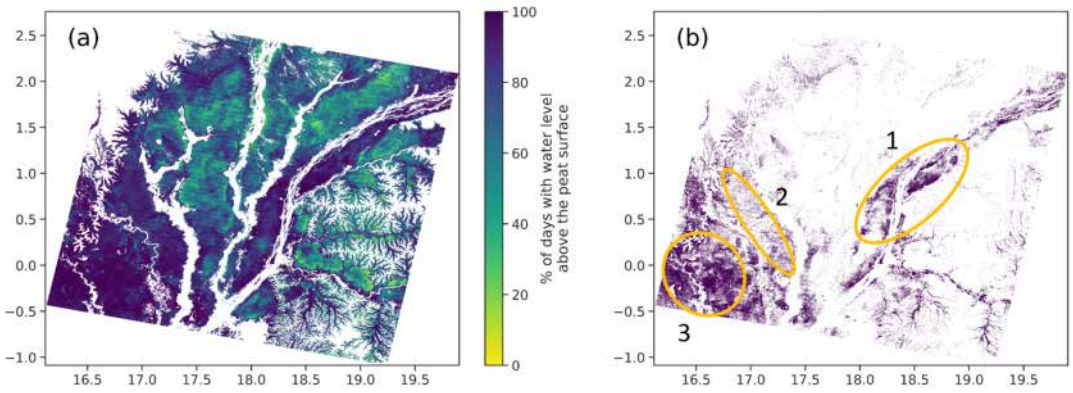

Figure 12. For peatland locations, (**a**) the percentage of days between March 2019 and October 2020 when the water level was at or above the peat surface and (**b**) locations where the water level was always at or above the peat surface—some examples include (1) a floodplain region, (2) an inter-fluvial rainfed region, (3) a large rainfed region in the southwest of the study area that was largely permanently inundated during this period.

3.6. Assessing the Relationship between Water Level Variation and Swamp Vegetation Type

We identified large differences between palm and hardwood swamp water levels for the mean value of the maximum water level, at 45% higher for palm swamp; the mean value of the mean water level, at 86% higher for palm swamp and the mean value of the standard deviation of the water level, at 33% higher for palm swamp (Table 2). The range of the mean HH backscatter calculated across all SAR image time steps largely overlaps between these two vegetation classes (Figure 13) and the differences between the water level mean, maximum and standard deviation values are likely to be representative of actual differences in water level between the two swamp vegetation types, rather than due to differences in backscatter from different vegetation cover.

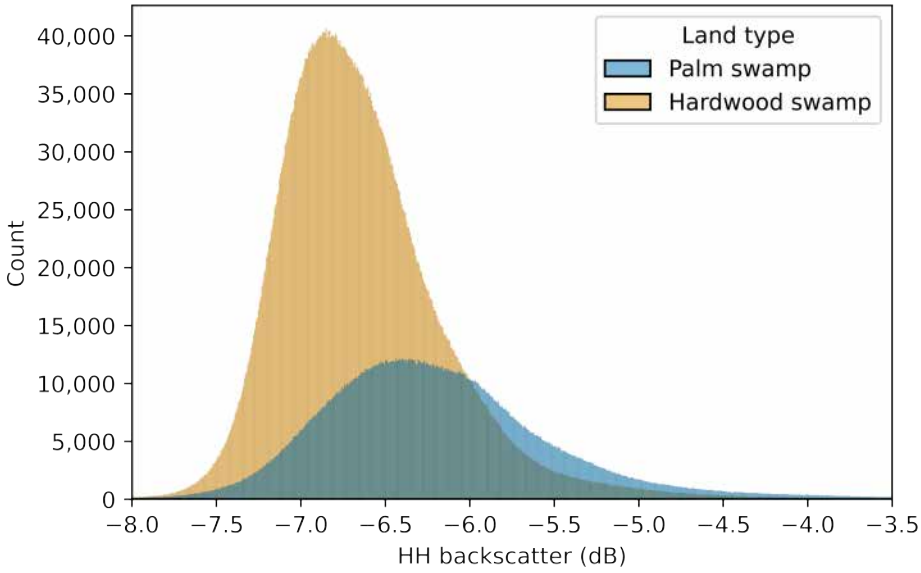

Figure 13. Distribution of mean HH polarisation backscatter across the PALSAR-2 image stack for palm and hardwood swamp types.

By comparison of swamp vegetation type (Figure 1b) and the maximum and standard deviation of the water level (Figure 11b,d), we observe similarities between the large-scale pattern of peat swamp type and the variability in the water level, with higher water levels in areas dominated by palm swamp. We summarise our comparisons between palm and

hardwood swamp for the minimum, maximum, mean and standard deviation metrics in Table 2.

Table 2. Statistics corresponding with the correlation between swamp vegetation type and water levels above the peat surface, calculated using ANOVA regression. The total sample size across the hardwood (HWS) and palm swamp (PS) land cover types is 8,646,611.

Metric Tested	ANOVA F-Stat	p-Value	η^2	Mean for HWS (cm)	Mean for PS (cm)
Minimum water level	2687	0.0	0.0003	−5.91	−5.72
Maximum water level	1,230,110	0.0	0.125	14.93	21.6
Mean water level	898,409	0.0	0.094	3.40	6.32
Std. dev. of water level	898,284	0.0	0.094	4.41	5.86

The ANOVA test η values show a low but significant correlation for the maximum, mean and standard deviation of the water level in relation to swamp vegetation type. While we only refer to the two principal swamp vegetation types, palm and hardwood, Crezee [33] concluded that there may be a further seasonally inundated vegetation type, located in the floodplain swamps to the east of the Congo River. The conditions favoured by this third class may contribute to some of the variability in water level statistics shown in Table 2.

3.7. Comparison between Modelled Water Level and Water Logger Data

In Figure 14, we compare the modelled and in situ water logger data for five water loggers located in two regions of the Cuvette Centrale: Lokolama in the DRC and Ekolongouma in the RoC (see Figure 9). The corresponding statistics are shown in Table 3. Kendall's τ statistics of >0.3 have been classified as strongly correlated [55], and we find that the statistics for all logger locations are significant to some degree and that the direction of the water level rise and fall is correlated between the modelled and logger recorded data. However, we find that the significance of their correlation is more variable with reference to their R^2 (0.22 to 0.56) and ρ values (0.47 to 0.73). This indicates that, although the direction of change in water levels is generally well represented within our model, the model has variable success in representing the magnitude of the change in water levels. The Ekolongouma (EKG) logger locations have the most significant pixel-wise correlation and model validation statistics (see Table 2).

The water loggers provide us with point information, whereas the PALSAR-2 data and the derived (modelled and interpolated) water levels are indicative of the average water level evolution within a 1-hectare area. Due to differences in the topography, the logger water levels may not be indicative of the wider pixel average water levels. We can see an example of this by comparing the time series of the two Ekolongouma water loggers, which are separated by only 1.7 km, but measure considerably different water levels (Figure 14). In this case, the modelled data more closely represents the actual water levels recorded by the EKG03 water logger. It is possible that the EKG02 logger was positioned in a hollow (a micro-topographical feature at a lower level than the surrounding terrain) which is, therefore, less likely to be representative of the water levels corresponding with the wider 1-hectare pixel area. Further, convective precipitation events resulting in higher localised daily rainfall totals when compared to the larger 0.05° × 0.05° area will not be well captured by the modelled water level time series. An example of this may be evident in November 2019 for the EKG03 logger time series, where the reducing water level modelled using the larger area CHIRPS rainfall data does not correspond well with the increase in water level in the Ekolongouma area.

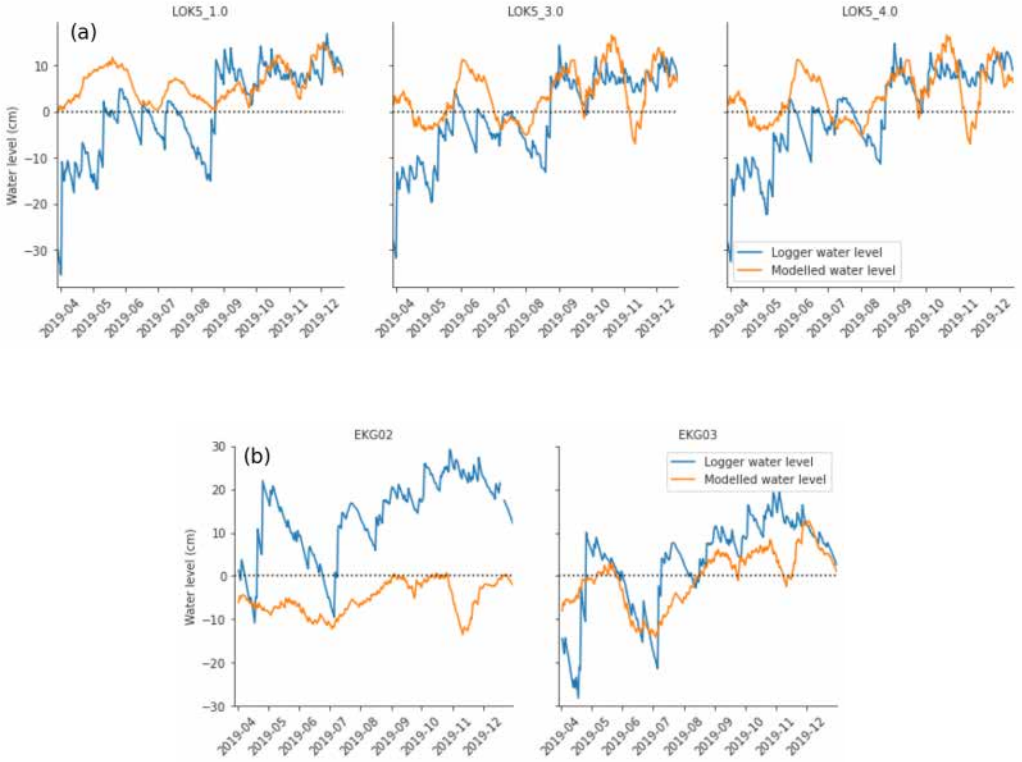

Figure 14. Comparison between modelled and logged water levels for (**a**) three sites in the Lokolama region of the DRC and (**b**) two sites in the Ekolongouma region of the RoC.

Table 3. Pixel-wise correlation statistics, calculated between the PALSAR-2 image stack and the net water accumulations; and the model validation statistics, calculated between the interpolated (modelled) water level data and the water logger data. The *p*-values corresponding with the model validation statistics are all <0.01 (not shown in the table). The first four logger locations in the table have pixel-wise correlation statistics with *p*-value < 0.15 (our threshold for using the rainfed algorithm) and the final one (LOK5_4.0) has a lower pixel-wise correlation with the net water input and, therefore, the modelled estimate of its water level used the linear interpolation method.

			Pixel-Wise Correlation Statistics				Model Validation Statistics		
Logger	**Latitude**	**Longitude**	R^2	***p*-Value**	**Slope (cm/dB)**	**Std Error (cm)**	R^2	**Kendall's τ**	**Spearman's ρ**
EKG02	1.191986	17.84694	0.37	0.01	7.53	2.85	0.41	0.45	0.63
EKG03	1.188695	17.83192	0.28	0.03	5.28	2.45	0.56	0.53	0.73
LOK5_1	−0.303200	18.20069	0.25	0.04	6.65	3.35	0.22	0.32	0.47
LOK5_3	−0.314950	18.18710	0.1	0.14	3.93	3.45	0.34	0.40	0.60
LOK5_4	−0.317950	18.18378	0.07	0.18	4.15	4.28	0.26	0.35	0.53

3.8. Comparison between Modelled Water Level and Altimetry Data

Figure 9 shows the locations of the four altimetry stations we use in these comparisons. Only one (KM1374) showed indications of being in a rainfed region, with significant pixel-wise correlation statistics. The water levels at the other locations are largely influenced by upstream hydrological dynamics, and, overall, they have a non-significant correlation with rainfall in their vicinity. The rainfed algorithm was therefore used only for the KM1374 altimeter, where there is an indication from the pixel-wise correlation statistics of some correlation with the net water input (R^2 = 0.26, *p*-value = 0.03). Linearly interpolated values were extracted for the other altimeter locations. Figure 15 shows a comparison between the temporal patterns of the derived water level data and the altimetry data, and Table 4 shows the corresponding statistics. The model validation statistics are significant at all locations.

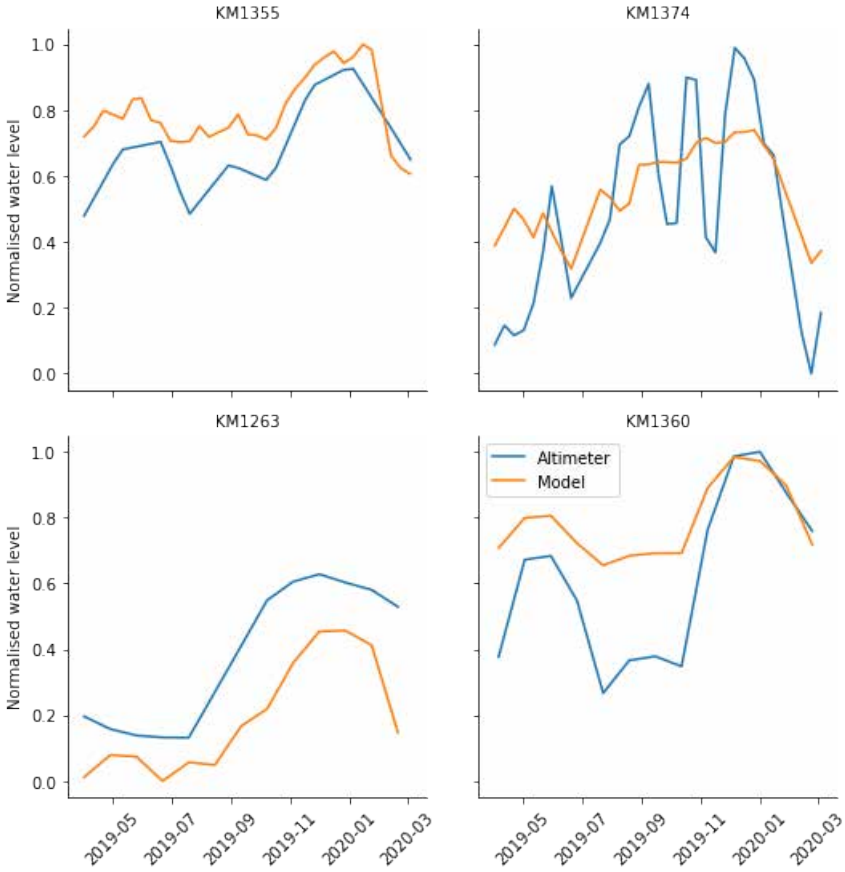

Figure 15. Comparison between the patterns of modelled and radar altimetry-derived water levels for four altimetry virtual station locations over peatland. KM1355 and KM1374 are from the Jason-3 altimeter (10-day repeat cycle), and KM1263 and KM1360 are from the Sentinel-3 altimeter (27-day repeat cycle). The locations of these virtual stations are shown in Figure 9.

Table 4. Pixel-wise correlation statistics, calculated between the PALSAR-2 image stack and the net water accumulations; and the model validation statistics, calculated between the interpolated (modelled) water level data and the available altimetry data over peatland areas corresponding with each altimeter location. The rainfed model was used for KM1374's location. Otherwise, the linear model was applied. The *p*-values corresponding with the modelled data validation statistics are all <0.01 (not shown in the table).

			Pixel-Wise Correlation Statistics				Model Validation Statistics		
Altimeter	**Latitude**	**Longitude**	R^2	***p*-Value**	**Slope (cm/dB)**	**Std Error (cm)**	R^2	**Kendall's τ**	**Spearman's ρ**
KM1355	−0.24	19.23	0.04	0.24	1.38	1.87	0.64	0.51	0.67
KM1374	0.36	19.01	0.26	0.03	1.89	0.92	0.58	0.54	0.74
KM1263	0.27	18.47	0.00	0.47	0.10	1.34	0.79	0.72	0.87
KM1360	−0.39	19.26	0.07	0.19	0.95	1.03	0.85	0.84	0.94

4. Discussion

In this section, we discuss the applicability of our methods and results in a broader context, as well as the relevance of our findings to our original research questions. We also address the limitations of our study and explore the potential for improved accuracy of the water level maps by incorporating additional remotely sensed data.

4.1. Applicability of the Modelled Water Level Maps

We generated daily water level maps with a resolution of 100 m (1 hectare) across the Cuvette Centrale region for a 20-month period from 29 March 2019 to 9 October 2020. These maps have various practical applications, which we describe here.

4.1.1. Facilitating Scaling Up of Methane and Carbon Dioxide Fluxes

Our study aimed to provide high-resolution water level maps that can help us to understand the spatiotemporal patterns of methane and carbon dioxide emissions from peatlands. By comparing the estimated water levels with in situ greenhouse gas measurements, it becomes possible to develop a transfer function for estimating fluxes at the regional scale.

4.1.2. Supporting Model Calibration and Validation

Lee et al. [15] produced water level maps for the central Congo Basin which corresponded with the availability of ALOS PALSAR satellite imagery. They suggested that these maps could be valuable for both validating and calibrating hydrodynamic models' representations of variations in water level and surface water extent. Our interpolation of the ALOS-2 PALSAR-2 HH backscatter data using the net water input provides the first high temporal (daily) resolution map of water level evolution over a region of the Cuvette Central peatlands, and these maps could be used within the development and assessment of hydrological models. Additionally, extending our study over a longer time frame would enable a more accurate assessment of spatiotemporal water level variations with net water input and a more accurate derivation of pixel-wise relationships. This, in turn, would facilitate estimating future changes in land surface water storage under different climate change scenarios. Given that the Congo Basin is on a climatic threshold [41], future changes in rainfall patterns could have significant implications for the peatlands' status as a carbon store, as well as impacting forest use and livelihoods.

4.1.3. Enhancing Understanding of Water Transfer between River Systems and Surrounding Wetlands at High Spatiotemporal Resolution

Previous hydrological mapping studies over the central Congo Basin have focussed on surface water extent (SWE) and storage (SWS). Frappart et al. [17] provide a comprehensive overview of these studies. Our generated maps allow for the calculation of SWS temporal evolution at a 100 m pixel level by multiplying water level with pixel area, accounting for tree stem area/density. For rainfed pixels, the water level at each pixel correlates with the net water input approximation, without considering groundwater inputs. For flood-prone pixels, the water transfer between the river system and the surrounding wetlands could be approximated by calculating the difference between the daily net water input (rainfall minus evapotranspiration) and the daily, linearly interpolated, HH backscatter-derived estimate of water level. This analysis would be valuable for understanding the daily, monthly and seasonal contributions of water transfer between the river system and the adjacent peatlands.

4.1.4. Forecasting Short-Term Water Level Changes

The period of maximum correlation metric (Table 1, fourth column) shows the potential to forecast water level changes in different regions. By using weather forecast outputs to determine the expected net water input in the coming days and weeks, Equation (1) could be used to forward interpolate the SAR backscatter data. The transfer equation we derived between σ_0 and water level (Equation (5)) could then be used to forecast water level for the time during which changes in the SAR backscatter remain correlated with net water accumulation for that location.

4.2. Our Results in the Context of the Original Research Questions

We began by posing three key research questions. Here, we discuss how our findings contribute to addressing these questions.

4.2.1. Distinguishing Rainfed and Flood-Prone Peatland Areas

The use of pixel-wise correlation statistics between the estimated net water input and the change in SAR backscatter between subsequent image dates proved useful for distinguishing between rainfed and flood-prone regions within our study area. The regions with the highest correlation, largely located in the inter-fluvial regions of the RoC and the southwest of the study area (Figure 6a), predominantly receive their net water input directly from rainfall. In contrast, areas along the banks of the Ubangui and Congo rivers, which are subject to flooding, have the lowest correlations.

Overall, we identified 72.5% of the study area as containing partially or fully rainfed peatlands. Significant correlations ($p < 0.05$) were calculated for 50% of the study area, indicating direct rainfed conditions, while a further 22.5% of the study area may be classed as being partially rainfed. Partially rainfed areas may experience flooding for a limited period, for example, during periods of intense or prolonged rainfall when local levees may be breached. Although the elevation of the Cuvette Centrale peatlands varies little (Figure A2a), sloped areas (Figure A2c) contribute to surface and sub-surface runoff and water pooling, especially during periods of heavy rainfall. Peatlands in these locations, even when isolated from river system inputs, were classified as partially rainfed in our study.

4.2.2. Spatial and Temporal Variation in Inundation across the Study Area

Approximately 27.5% of 1-hectare pixels in our study area showed no correlation between net water input and changes in SAR backscatter/water levels. The majority of these pixels are located in the flood-prone peatland areas to the east of the Congo River and between the Congo and Ubangui rivers. In these areas, there is a time lag between increases in rainfall and subsequent water level rise, as it can take 1 to 3 months for the increased water input upstream to contribute to riverine flooding downstream [50]. Lagged correlations were not explored in this study. We observed the highest water level amplitudes in these flood-prone locations. This is likely due to combined rainfall and floodwater inputs during the wet season leading to high water levels, while during drier periods, the receding floodwaters and rainfall inputs are channelled into the river system via the same pathways from which they receive flood inputs.

Lee et al. [15] used differential interferograms to examine water level changes in the Cuvette Centrale using two sets of fine-beam ALOS PALSAR scenes. They found distinct spatial variations in fringe patterns, observing densely packed fringes along the Congo mainstem, while the inter-fluvial regions had broader and more diffuse patterns. These findings suggested different hydrological input/flow mechanisms between the two regions and are in agreement with our categorisations of rainfed and flood-prone areas.

Our study period included the impacts of an extended heavier-than-normal rainfall event between October 2019 and January 2020, resulting in elevated water levels (see Figures A5 and A6). Under climatological rainfall conditions, some areas would not experience the same degree of flood inputs and would be classified as directly rainfed for a greater portion of the year. A longer time series of PALSAR-2 data would enable an assessment of seasonal pixel-wise correlations and enhance our understanding of the seasonality of rainfed versus flood-prone classifications.

Water level variability was 5 to 70 cm at the 1 ha scale, with maximum variations in the flood-plain areas and a mean water level amplitude of 22.8 $\pm$ 10.1 cm to 1 standard deviation. These variations are close to the seasonal variability estimated by Lee et al. [15] of 20 to 60 cm over flooded forest areas that they derived using a single altimetry track over the Cuvette Centrale for the years 2002 to 2010. Additionally, using ALOS PALSAR ScanSAR data, Lee et al. [15] estimated maximum water levels of 1 to 1.5 m along a narrow fluvial region bordering the Congo mainstem, while an inter-fluvial region between the

Congo River mainstem and the Ubangui/Ngiri rivers had shallower water levels of up to 60 cm.

By applying our methods to ALOS-2 PALSAR-2 data available over the longer term, we will be able to better constrain the long-term water level variability across the Cuvette Centrale.

4.2.3. Distinct Optimal Water Levels for Different Swamp Vegetation Types

Our analysis of water level metrics in relation to peatland vegetation type showed significantly higher mean, maximum and standard deviation values of water level for palm swamp pixels in comparison to hardwood swamp. This suggests palm swamps have a preference for locations with higher rainfall and inundation levels. However, due to the significantly wetter wet season in our study period compared to the climatological average, we were unable to assess the seasonal correlation between minimum water level and swamp vegetation type. It is possible that everywhere met the minimum water requirements to suit all swamp vegetation types. To better quantify the optimal inundation levels and duration for each swamp type, it would again be beneficial to generate inundation maps over a longer time period and across the entire Cuvette Centrale. For instance, in our current study area, most palm swamp regions are situated west of the Congo River (in the RoC and northern DRC). However, another extensive region of palm swamp is located south of our study area, in the DRC floodplains, which receive significantly higher rainfall inputs in addition to flood inputs. Calculating mean water level statistics for palm and hardwood swamp vegetation types across this wider region would allow us to determine if there is an upper limit on inundation extent or water level for palm swamps. By improving our understanding of this, we will be better equipped to assess the potential impact of future climate change on the current distribution of swamp vegetation. Additionally, Crezee [33] found indications of a third seasonally flooded peat swamp vegetation type, principally located in the floodplain regions of the DRC, but which had not yet been accounted for in landcover maps. Its distribution should be taken into account when examining the water level preferences of different peat vegetation types.

4.2.4. Differences in Peatland Hydrological Inputs to the East and West of the Congo River

We identified the most directly rainfed peatland areas in the RoC to the west of the Congo River and in the northern part of the DRC region between the Congo and Ubangui rivers (Figure 7a). Conversely, the most flood-prone peatland regions were situated east of the Congo River and surrounding the Congo mainstem (Figure 7b). These differences in sources of hydrological input to the east and west of the Congo River can be attributed to variations in levee heights between the river, its tributaries and the surrounding peatland regions. To illustrate this, Figure 16 shows a map of the Relative Topographic Position Index (RTPI) covering peatland pixels within our study region. Comparing the pixel-wise correlation in Figure 6a with the RTPI, we observe that areas with the lowest correlation correspond to locations along the banks of the Ubangui and Congo rivers, where the RTPI is closest to zero, indicating that the river banks in these locations are closer to the level of the surrounding terrain. We observe higher levees along the banks of the Sangha and Ubangui rivers. We also observe that the majority of the area composed of hardwood swamps to the east of the Congo River has RTPI values below zero, indicating that its peatlands are hydrologically linked to the main river system via tributaries. In contrast, the neighbouring palm swamp regions have RTPI values above zero, indicating a higher likelihood of being directly rainfed and less susceptible to floodwater inputs.

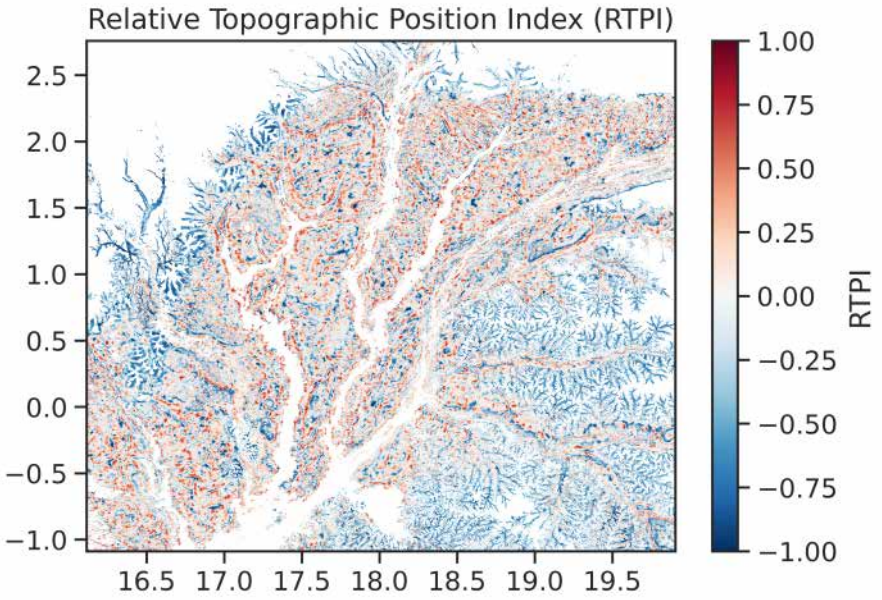

Figure 16. The Relative Topographic Position Index (RTPI), the relative difference in elevation between a pixel and its surrounding neighbours, is derived from the MERIT 90 m DEM using a 56 × 56 filter kernel. Its values are masked to show only peatland areas. Positive values indicate that an area is elevated relative to its neighbours and negative values indicate that an area is on a lower level.

4.3. Accuracy of Interpolated Inundation Maps and Limitations

The pattern of the temporally interpolated data in rainfed regions follows that of the daily net water input. While all locations receive some contribution to their groundwater storage from the daily net water input at that location, regions that receive additional water inputs from river flooding will have a time-lag component [50] corresponding with the delay in upstream rainfall contributing to downstream flooding. In flood-prone regions, our linear interpolation between PALSAR-2 dates, which are mostly separated by 42 days, fails to capture the shorter-term fluctuations resulting from the combined variations in the rainfall patterns both upstream and at the given floodplain pixel. As a result of applying a pixel-wise correlation threshold, 72.5% (Figure 6d) of peatland pixels within our study region have had their daily water levels modelled using the rainfed algorithm.

In flood-prone regions, the higher temporal resolution of Sentinel-1 C band data could be used in conjunction with the ALOS-2 PALSAR-2 data to better capture shorter-range temporal changes in flooding. This would be especially applicable along the edges of rivers where there is less dense swamp vegetation limiting the shorter wavelength C-band signal from resolving changes in water level over the peat surface.

Additionally, flood models that are based on river hydrodynamics would be useful for infilling or complementing the water level maps in floodplain areas.

4.4. Microtopography Considerations

The landscape is characterised by spatial variations in the distribution of vegetation and root systems, resulting in a series of tree roots/hummocks (dryer elevated regions) with depressions (hollows) in between where water pooling can occur. These features can vary over spatial scales of less than 2 m. However, the SAR data we used is at 100 × 100 m resolution after speckle filtering, which is not high enough to capture such micro-topographical features and may, therefore, underestimate the highest flood levels while overestimating the lowest ones. Additionally, the water-logger depth measurements used to validate the SAR data may have been taken in hollows, on hummocks or in an area that is not representative of the average elevation of the surrounding area. We see indications of this in the comparisons with the in situ water logger data. To address this,

we recommend that future placement of water loggers should be at a level approximately equal to the average terrain level in the surrounding hectare region. This approach would facilitate a more direct comparison between logger measurements and satellite instrument measurements, which reflect the mean conditions of water level or other environmental parameters over a larger area. Additionally, a larger-scale network of water loggers would be beneficial.

4.5. Recommendations for Enhancing Map Accuracy

Our interpolation of the HH backscatter to daily resolution was performed at 1 ha resolution, using the relationship calculated between the backscatter and the net water input at each pixel. The pixel-wise linear regressions were calculated across the whole time series and covered all seasons. However, due to the non-linear hydrological dynamics in many locations, the slope of the relationship between the backscatter and the net water input is likely to vary seasonally. For example, a location that is primarily rainfed may receive additional inputs from groundwater flow or runoff during the wettest periods, or some pixels may be considered rainfed for most of the year but receive floodwater inputs during the wettest season. Accounting for these variations could be achieved by using the full time-series of PALSAR-2 data available since 2014, calculating seasonal pixel-wise correlations and applying the resulting varying relationships to the interpolation of the HH backscatter.

The daily water level maps include a period that was significantly wetter than the climatological average. By calculating the water level metrics for each pixel (minimum, maximum, mean, amplitude and standard deviation) over a longer-term period, we could produce climatologies of the expected water level variations at each pixel.

In our study, we used daily 0.05° resolution rainfall data, which captures mesoscale rainfall variability well. However, it is important to note that this resolution cannot capture microscale convective storm events, potentially resulting in the omission of short-term high rainfall occurrences. Higher-resolution rainfall data would help to address this.

Currently, there is a lack of sufficient virtual altimetry station data coverage over peatland locations, which limits comprehensive validation of the peatland water levels we derived. However, the recently launched Surface Water and Ocean Topography (SWOT) mission [56,57] will help to address this gap. The SWOT mission uses interferometric altimetry at Ka-band to measure both land and ocean water surface topography at high spatial resolution and its measurements are available as gridded global datasets [56]. In future studies, these data could be used to validate SAR-derived water level estimates, particularly over some of the less vegetated, floodplain regions of the Cuvette Centrale.

5. Conclusions

We have presented a method for combining the daily pattern of net water input with high-resolution L-band SAR data to estimate daily, 100 m resolution time series of water levels across a largely rainfed region of the Cuvette Centrale tropical peatland complex. We have also introduced a technique for distinguishing between rainfed and flood-prone areas. We show that 50% of the region is directly rainfed, while 22.5% is partially rainfed. The remaining 27.5% is located in floodplains or locations that receive significant groundwater input and have a low correlation with direct rainfall. With the recent open release of ALOS-2 PALSAR-2 level 2.2 ScanSAR data, the methods we describe can be adapted and applied across the entire peatland complex from 2014 to the present, allowing for higher-resolution estimates of water levels, inundation extents and surface water storage evolution. This is important because carbon accumulation in the peatlands is sensitive to surface-water levels. By mapping long-term water level variations and their relationship to net water input, we will be better equipped to understand the impact of climate change on the region's inundation patterns. Such an improved understanding can contribute to assessing the future security of the peatland complex as a carbon store.

Author Contributions: Conceptualisation, S.G. and E.T.A.M.; Data curation, S.G., B.C., G.C.D., D.M.Y., A.J.J.-S., B.K. and F.P.; Formal analysis, S.G.; Funding acquisition, E.T.A.M. and S.L.L.; Investigation, S.G., B.C., G.C.D., Y.E.B., P.B., D.E.C., O.B.E., C.E.N.E., N.T.G., J.T.K., Y.E.W.M., M.M. and J.-B.N.N.; Methodology, S.G. and E.T.A.M.; Project administration, E.T.A.M. and S.L.L.; Resources, E.T.A.M., C.E.N.E., S.A.I., P.I.P., S.S. and S.L.L.; Software, S.G.; Supervision, E.T.A.M.; Validation, S.G.; Visualisation, S.G.; Writing—original draft, S.G.; Writing—review & editing, S.G., E.T.A.M., B.C., G.C.D., D.M.Y., B.K., F.P., P.I.P., S.S. and S.L.L. All authors have read and agreed to the published version of the manuscript.

Funding: Funding for this research was provided by the Natural Environment Research Council (NERC) through an E4 DTP studentship (NE/S007407/1), the CongoPeat grant (NE/R016860/1; https://congopeat.net), which provided co-authors with full or partial financial support, and Paul I. Palmer received support from the UK National Centre for Earth Observation (NE/R016518/1).

Data Availability Statement: The code developed within this research and links to the water level map are available at: https://github.com/SelenaGeo/InundationMapping/, last accessed 9 June 2023.

Acknowledgments: We would like to thank Helen Plante at Leeds University for providing excellent administrative and translation assistance related to this research. We also thank all the software developers of open-source Python packages that enabled us to carry out this research efficiently, to the developers of openly available meteorological and terrain data sets used within this study and to ESA and NASA who have provided their satellite data under open-source terms for production of the altimetry virtual stations we used.

Conflicts of Interest: The authors declare no conflict of interest.

Appendix A

Appendix A.1. Post-Processing Applied to ALOS-2 PALSAR-2 Scenes

We used the European Space Agency (ESA) SNAP software and the Snappy Python interface package to apply the majority of the necessary post-processing steps detailed in Figure 3 to the SAR scenes as follows:

1. We converted the CEOS format SAR images into BEAM–DIMAP format, the default format used to produce all outputs when using SNAP, and separated the HH and HV polarisation bands into individual files such that the post-processing steps could be applied to each band individually;
2. Due to some small location differences in the footprint of each co-located scene, it was necessary to stack the images multi-temporally, defining a single image (the first date) as the one to which all the other images were aligned. Within the radar co-registration process, we specified product geolocation as the initial offset method and used a nearest neighbour resampling method;
3. Speckle is a feature of SAR images that results from coherent backscatter from multiple targets, leading to a granular appearance. We applied the Improved Lee Sigma speckle filter [52] to each individual image in the co-registered stack. This is recommended when assessing the temporal evolution of surface-water inundation, as multi-temporal speckle filtering could dampen the signal of seasonal variations too much. The Improved Lee Sigma filter is commonly applied to SAR data as it reduces blurriness [58]. It takes into account possible edges where the local variance around a pixel exceeds a certain threshold and is used to remove coherent noise. It is important to note that speckle filtering comes at the expense of image resolution. For the additional filter settings, we used a single look option and ran the process within a moving 7 × 7 window with resampling performed over a smaller target 3 × 3 window within this domain. The 7 × 7 window was used to detect whether an area contained speckle or realistic structures, and then the speckle filtering was applied over a smaller 3 × 3 window. Lee et al. [52] found that a 3 × 3 target window gave good results specifically with ALOS PALSAR data. Additionally, we used the default sigma value of 0.9;

4. Due to variations in the incident angle across the longitude axis of the PALSAR-2 imagery, of between 25.6° and 49.1°, there was an antenna pattern effect that required correction. The mean latitudinal backscatter values decreased linearly across the image extent from the satellite's position, corresponding with the linear increase in incident angle. To correct this, we performed the following steps:
   (a) Identified and masked permanent water bodies by applying a threshold of −11 dB to the backscatter. This value was arrived at by observing the backscatter over the time series for the lake and river bodies within the study area and is in agreement with the value used by Kim et al. [53];
   (b) Calculated the mean latitudinal backscatter across the full longitudinal extent of each image within the stack;
   (c) Calculated a linear regression across these values;
   (d) We applied this correction on an image-by-image basis due to environmental or SAR instrument differences that affect backscatter amplitude. However, it was also important that the slope of the antenna pattern correction applied is the same for all images, such that we could later analyse temporal changes in backscatter on a pixel-by-pixel basis. Temporal changes in hydrology impact the antenna pattern correction slope. We calculated the average slope of the linear regression across all time steps and applied a unique intercept value for each image that maintained the original backscatter values at pixels with the lowest incident angle;
   (e) We defined the reference backscatter amplitude to be at the lowest incident angle (closest to the satellite). We calculated the difference between this value and the regression line values across longitude. Finally, we added these differences to the original averaged backscatter values at each longitude to arrive at an antenna-pattern corrected image;
   (f) We visually inspected each corrected image in the stack to ensure that the backscatter pattern was balanced.

   This effectively acted to rotate the pattern of each image's backscatter values across longitude, using the longitude with the lowest incident angle as the pivot point. The east-to-west backscatter patterns in the resulting images are noticeably more balanced;
5. The original resolution of the ALOS-2 PALSAR-2 scenes was 25 m but the effective resolution was reduced following the application of the speckle filter. We geocoded the scenes within the co-registered stack to 100 m resolution using the SAR-Mosaic function with a bilinear resampling option. The final geocoded product was in the WGS84 projection;
6. To express the data in units of decibels (dB), we applied the Sigma nought (σ_0) backscatter calculation across each image within the co-registered stack, using the following equation:

$$\sigma_0 = 10 * log_{10} DN^2 + calibration factor \quad \text{(A1)}$$

   where DN is the digital number value of the amplitude, or DN^2 is that of the intensity, and the calibration factor specific to ALOS-2 PALSAR-2 level 1.5 SAR data is −83 dB;
7. We then calculated the ratio HH:HV (HH−HV when calculated in dB), a metric that we used to test its usefulness for assessing water level changes.

Appendix B

Appendix B.1. Data Collected along Transects

Table A1. Summary of the transects along which water table depth, co-located with methane flux samples, were taken. Included are the date range of the sampling expedition along each transect and the number of samples taken for each of the dry and wet seasons. The dry and wet season sampling categorisation is representative of the climatological season and not of the actual water level conditions experienced in the region at the time.

Transect Name	Country	Dry Season	Wet Season	Sampling Dates
Boboka	DRC	23	0	26 January–9 February 2020
Bondzale	RoC	24	0	4–6 March 2019
Ekolongouma	RoC	30	0	15–22 February 2019
Ikelemba	DRC	15	0	17–19 January 2020
Ipombo	DRC	30	29	Three sampling periods: 1. 13–15 March 2020 (dry) 2. 15–17 September 2020 (dry) 3. 27–30 October 2020 (wet)
Itanga	RoC	24	0	10–11 March 2019
Lobaka	DRC	29	0	21 February–3 March 2020
Lokolama	DRC	0	23	10–13 October 2020
Mpeka	DRC	35	40	Two sampling periods: 1. 18 June–1 July 2019 (dry) 2. 19–24 October 2020 (wet)
Totals		**210**	**92**	**All measurements: 302**

Appendix B.2. Water Logger Data Summary

Table A2. Summary of the available water logger data corresponding with our study period.

Location	Water Logger Name	Start Date	End Date	Lat	lon	Corrected?
GEM	EKG02	16 March 2019	21 March 2021	1.191986	17.84694	Y
GEM	EKG03	15 March 2019	17 March 2021	1.188695	17.83192	Y
Lokolama	LOK5_1.0	1 February 2018	21 December 2019	−0.3032	18.20069	Y
Lokolama	LOK5_3.0	1 February 2018	21 December 2019	−0.31495	18.1871	Y
Lokolama	LOK5_4.0	1 February 2018	21 December 2019	−0.32095	18.18046	Y

Appendix B.3. ALOS-2 PALSAR-2 Summary

Table A3. Summary of the ALOS-2 PALSAR-2 image stack used within this research.

Date	Scene ID	Centre lat	Centre long	Shift	Area	Zone
29 March 2019	ALOS2261753600-190329	0.872	17.817	0	2	33
10 May 2019	ALOS2267963600-190510	0.871	17.818	0	2	33
21 June 2019	ALOS2274173600-190621	0.857	17.814	0	2	33
19 July 2019	ALOS2278313600-190719	0.872	17.819	0	2	33
30 August 2019	ALOS2284523600-190830	0.872	17.82	0	2	33
11 October 2019	ALOS2290733600-191011	0.873	17.821	0	2	33
22 November 2019	ALOS2296943600-191122	0.873	17.821	0	2	33
3 January 2020	ALOS2303153600-200103	0.873	17.821	0	2	33
14 February 2020	ALOS2309363600-200214	0.873	17.817	0	2	33
27 March 2020	ALOS2315573600-200327	0.872	17.816	0	2	33
8 May 2020	ALOS2321783600-200508	0.871	17.821	0	2	33
19 June 2020	ALOS2327993600-200619	0.857	17.817	0	2	33
17 July 2020	ALOS2332133600-200717	0.857	17.817	0	2	33
28 August 2020	ALOS2338343600-200828	0.872	17.821	0	2	33
9 October 2020	ALOS2344553600-201009	0.872	17.821	0	2	33
8 October 2021	ALOS2398373600-211008	0.873	17.82	0	2	33
19 November 2021	ALOS2404583600-211119	0.874	17.821	0	2	33

Appendix B.4. Additional Figures

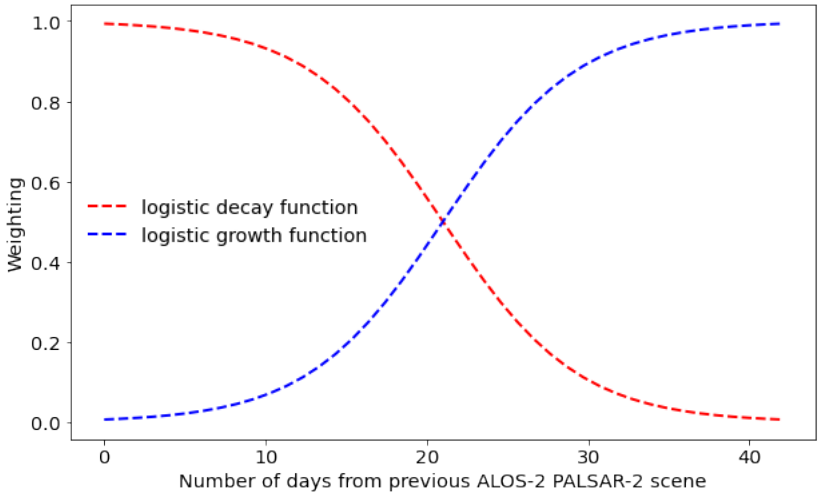

Figure A1. The logistic function growth and decay functions applied to the forward- and backward-calculated interpolated daily HH time series to arrive at a final HH daily time series.

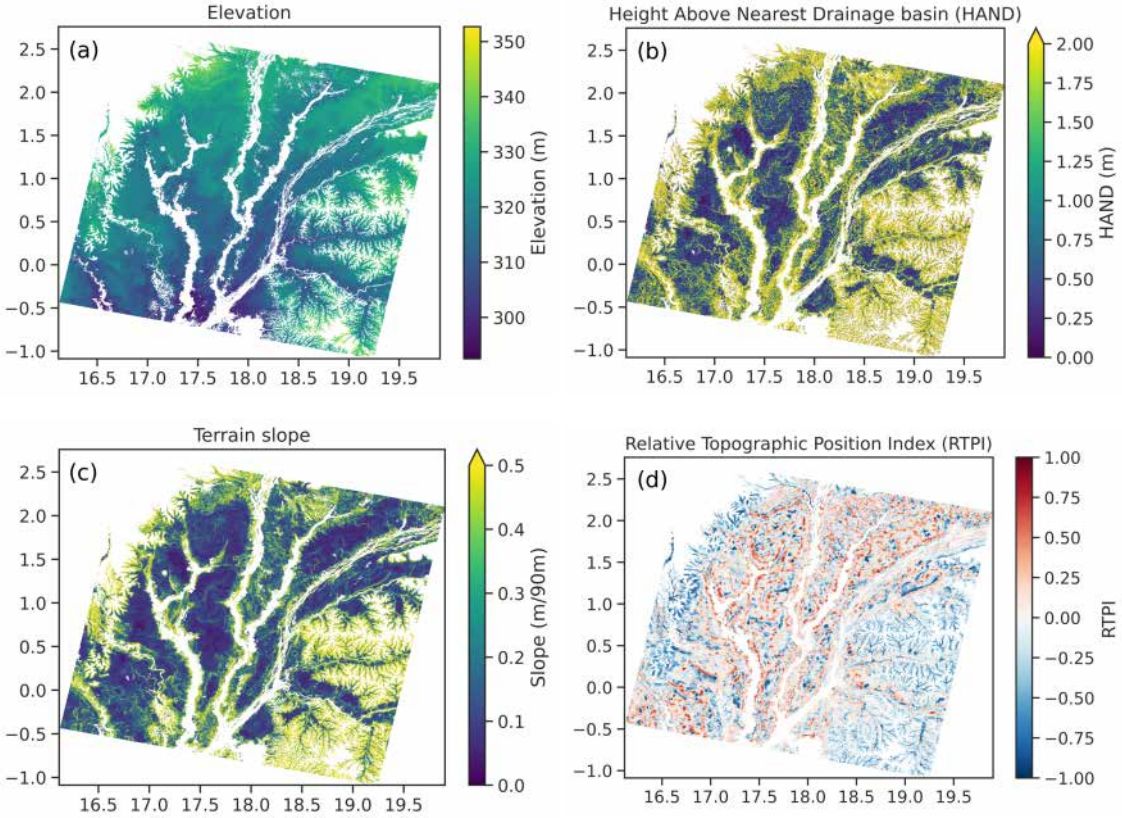

Figure A2. Terrain characteristics corresponding with peatland pixels that lie within the extent of our PALSAR-2 study region. (**a**) MERIT Hydro elevation, (**b**) MERIT Hydro height above nearest drainage basin (HAND), (**c**) slope, derived from the MERIT DEM, (**d**) the relative topographic position index (RTPI), also derived from the MERIT DEM.

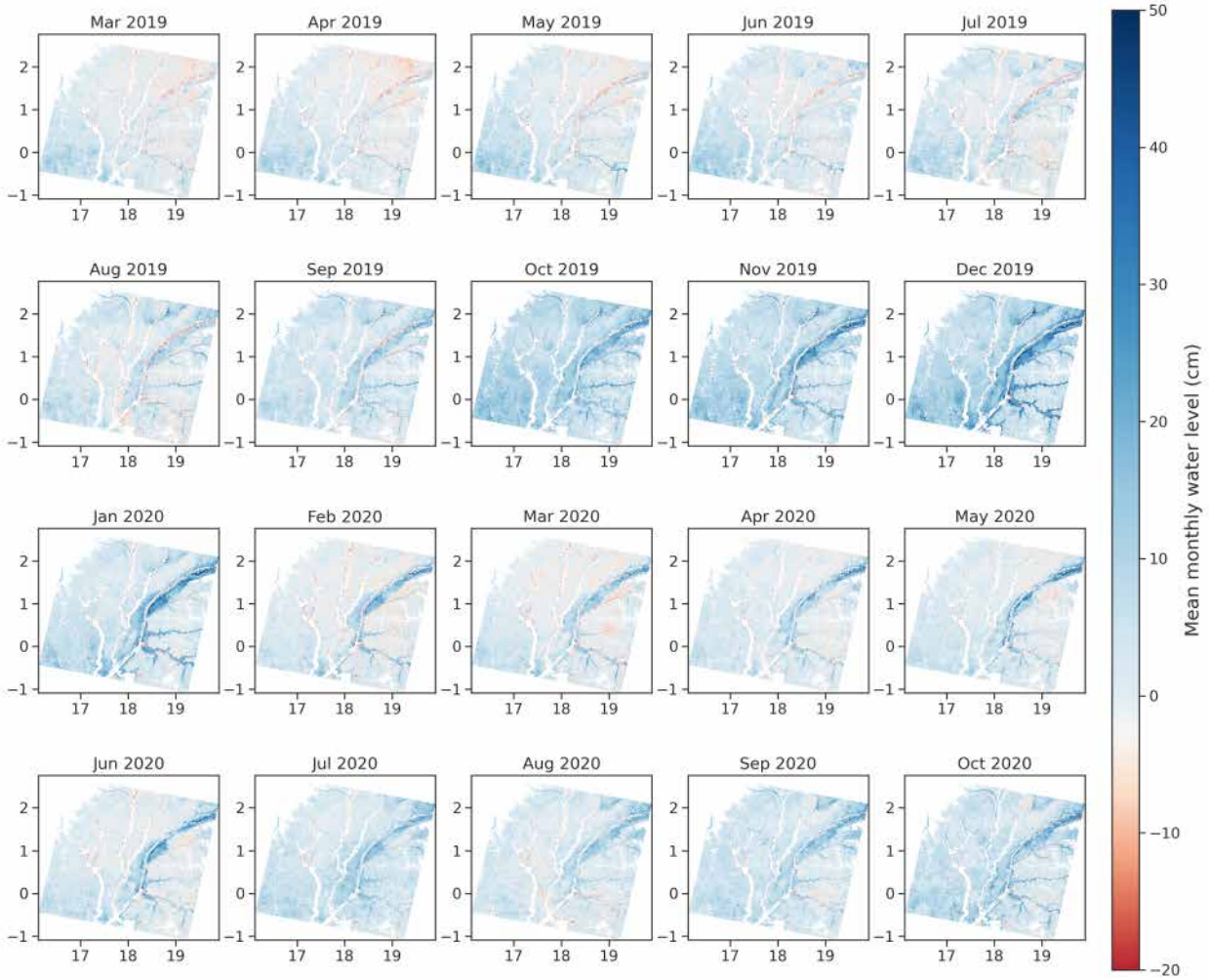

Figure A3. The modelled mean monthly water levels for locations with peat swamp land cover types.

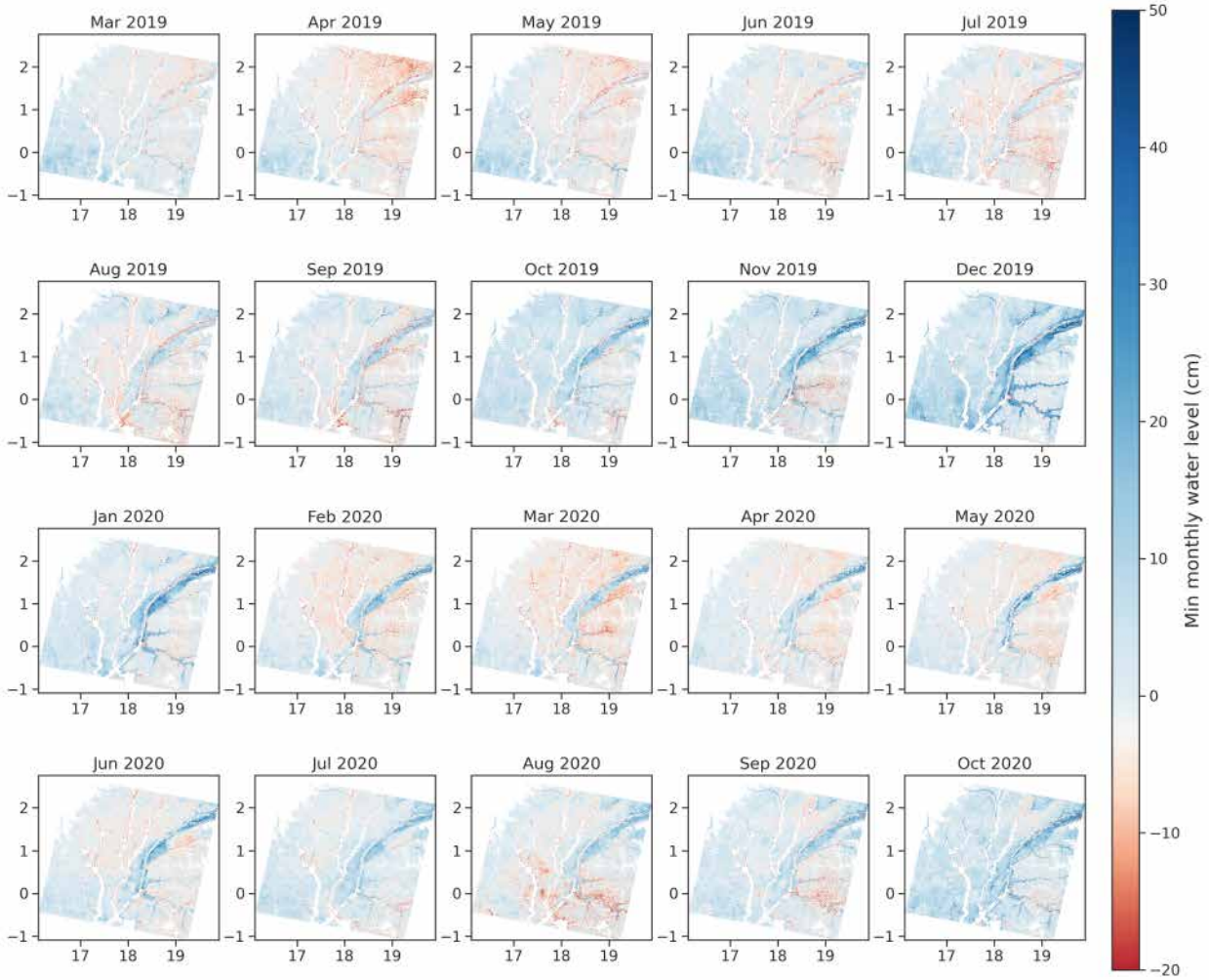

Figure A4. The modelled minimum monthly water levels for locations with peat swamp land cover types.

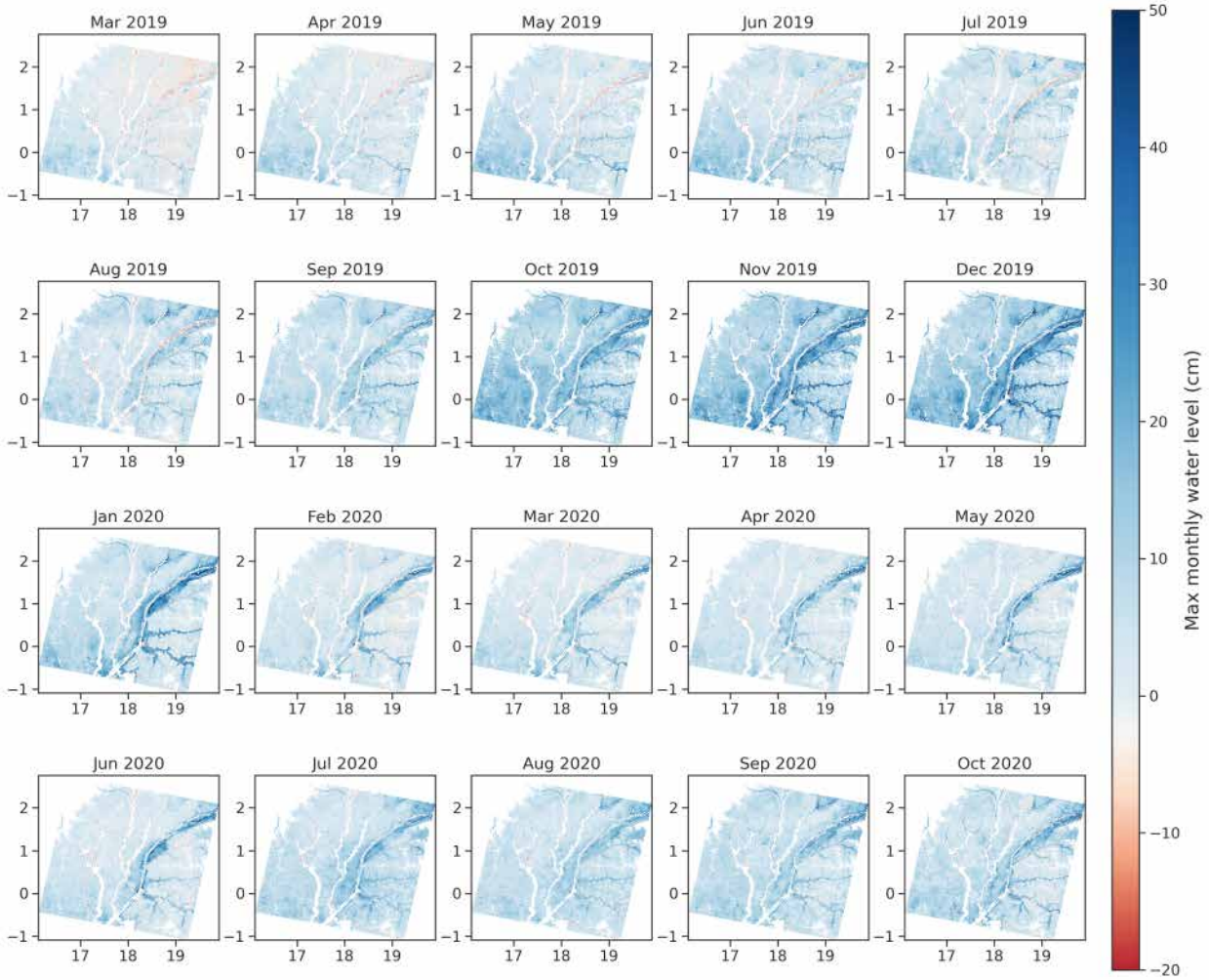

Figure A5. The modelled maximum monthly water levels for locations with peat swamp land cover types.

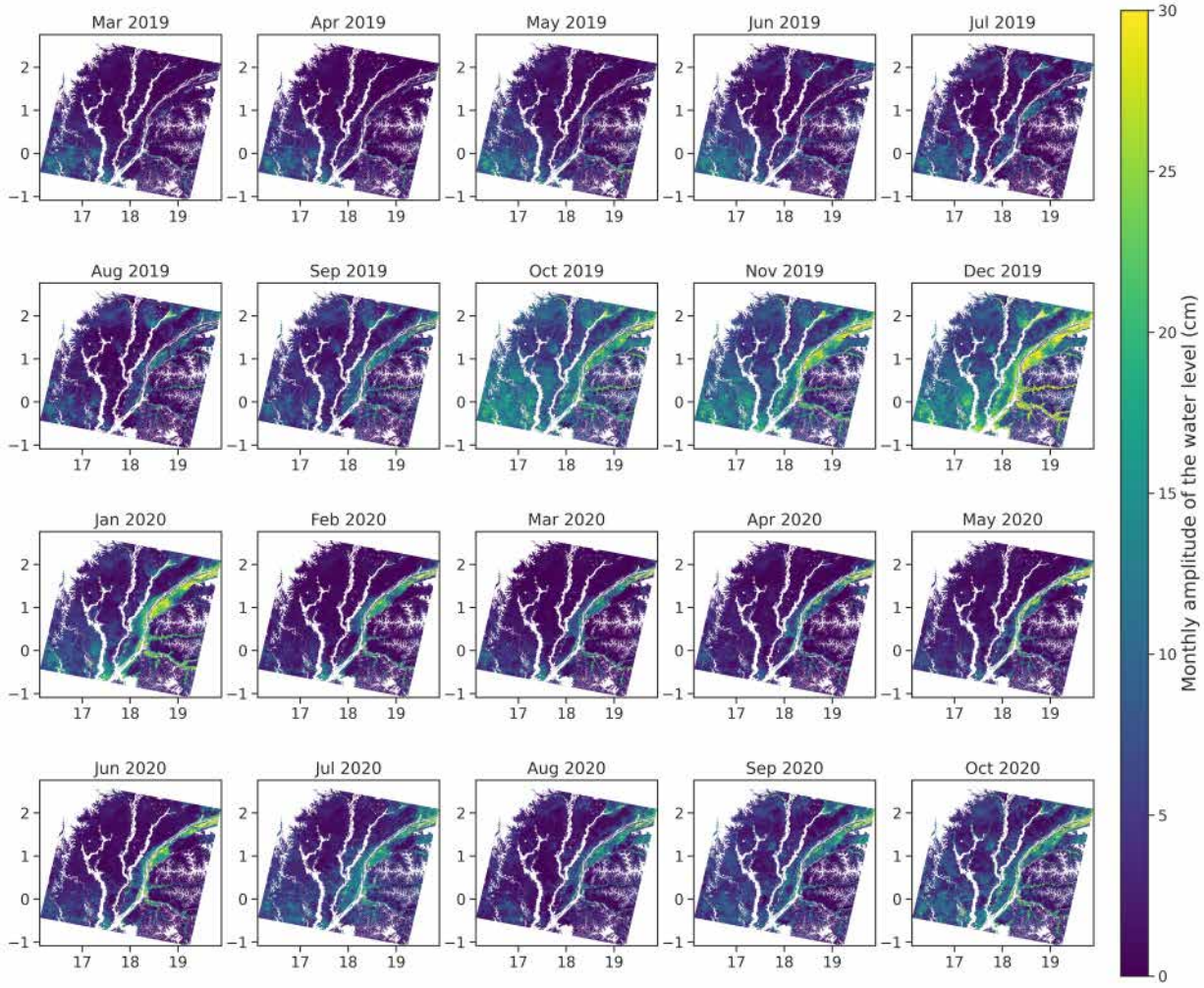

Figure A6. The amplitude (maximum−minimum) of the monthly water levels for locations with peat swamp land cover types.

References

1. Davidson, N.C.; Fluet-Chouinard, E.; Finlayson, C.M. Global extent and distribution of wetlands: Trends and issues. *Mar. Freshw. Res.* **2018**, *69*, 620–627. [CrossRef]
2. Mitsch, W.J.; Bernal, B.; Nahlik, A.M.; Mander, Ü.; Zhang, L.; Anderson, C.J.; Jørgensen, S.E.; Brix, H. Wetlands, carbon, and climate change. *Landsc. Ecol.* **2013**, *28*, 583–597. [CrossRef]
3. Junk, W.J.; Brown, M.; Campbell, I.C.; Finlayson, M.; Gopal, B.; Ramberg, L.; Warner, B.G. The comparative biodiversity of seven globally important wetlands: A synthesis. *Aquat. Sci.* **2006**, *68*, 400–414. [CrossRef]
4. Bousquet, P.; Ciais, P.; Miller, J.B.; Dlugokencky, E.J.; Hauglustaine, D.A.; Prigent, C.; van der Werf, G.R.; Peylin, P.; Brunke, E.G.G.; Carouge, C.; et al. Contribution of anthropogenic and natural sources to atmospheric methane variability. *Nature* **2006**, *443*, 439–443. [CrossRef]
5. Poulter, B.; Bousquet, P.; Canadell, J.G.; Ciais, P.; Peregon, A.; Saunois, M.; Arora, V.K.; Beerling, D.J.; Brovkin, V.; Jones, C.D.; et al. Global wetland contribution to 2000–2012 atmospheric methane growth rate dynamics. *Environ. Res. Lett.* **2017**, *12*, 094013. [CrossRef]
6. Zhang, Z.; Zimmermann, N.E.; Calle, L.; Hurtt, G.; Chatterjee, A.; Poulter, B. Enhanced response of global wetland methane emissions to the 2015–2016 El Niño-Southern Oscillation event. *Environ. Res. Lett.* **2018**, *13*, 074009. [CrossRef]
7. Zhang, Z.; Fluet-Chouinard, E.; Jensen, K.; McDonald, K.; Hugelius, G.; Gumbricht, T.; Carroll, M.; Prigent, C.; Bartsch, A.; Poulter, B. Development of the global dataset of Wetland Area and Dynamics for Methane Modeling (WAD2M). *Earth Syst. Sci. Data* **2021**, *13*, 2001–2023. [CrossRef]
8. Whalen, S.C. Biogeochemistry of methane exchange between natural wetlands and the atmosphere. *Environ. Eng. Sci.* **2005**, *22*, 73–94. [CrossRef]

9. Bergamaschi, P.; Frankenberg, C.; Meirink, J.F.; Krol, M.; Dentener, F.; Wagner, T.; Platt, U.; Kaplan, J.O.; Körner, S.; Heinmann, M.; et al. Satellite charactography of atmospheric methane from SCIAMACHY on board ENVISAT: 2. Evaluation based on inverse model simulations. *J. Geophys. Res. Atmos.* **2007**, *112*, D02304. [CrossRef]
10. Ringeval, B.; De Noblet-Ducoudré, N.; Ciais, P.; Bousquet, P.; Prigent, C.; Papa, F.; Rossow, W.B. An attempt to quantify the impact of changes in wetland extent on methane emissions on the seasonal and interannual time scales. *Glob. Biogeochem. Cycles* **2010**, *24*, GB2003. [CrossRef]
11. Dargie, G.C.; Lewis, S.L.; Lawson, I.T.; Mitchard, E.T.; Page, S.E.; Bocko, Y.E.; Ifo, S.A. Age, extent and carbon storage of the central Congo Basin peatland complex. *Nature* **2017**, *542*, 86–90. [CrossRef]
12. Ribeiro, K.; Pacheco, F.S.; Ferreira, J.W.; de Sousa-Neto, E.R.; Hastie, A.; Krieger Filho, G.C.; Alvalá, P.C.; Forti, M.C.; Ometto, J.P. Tropical peatlands and their contribution to the global carbon cycle and climate change. *Glob. Change Biol.* **2021**, *27*, 489–505. [CrossRef]
13. Couwenberg, J.; Dommain, R.; Joosten, H. Greenhouse gas fluxes from tropical peatlands in south-east Asia. *Glob. Change Biol.* **2010**, *16*, 1715–1732. [CrossRef]
14. Tshimanga, R.M.; Hughes, D.A. Basin-scale performance of a semidistributed rainfall-runoff model for hydrological predictions and water resources assessment of large rivers: The Congo River. *Water Resour. Res.* **2014**, *50*, 1174–1188. [CrossRef]
15. Lee, H.; Yuan, T.; Jung, H.C.; Beighley, E. Mapping wetland water depths over the central Congo Basin using PALSAR ScanSAR, Envisat altimetry, and MODIS VCF data. *Remote Sens. Environ.* **2015**, *159*, 70–79. [CrossRef]
16. Lee, H.; Jung, H.C.; Yuan, T.; Beighley, R.E.; Duan, J. Controls of Terrestrial Water Storage Changes Over the Central Congo Basin Determined by Integrating PALSAR ScanSAR, Envisat Altimetry, and GRACE Data. In *Remote Sensing of the Terrestrial Water Cycle*; Wiley Online Library: Hoboken, NJ, USA, 2014. [CrossRef]
17. Frappart, F.; Zeiger, P.; Betbeder, J.; Gond, V.; Bellot, R.; Baghdadi, N.; Blarel, F.; Darrozes, J.; Bourrel, L.; Seyler, F. Automatic detection of inland water bodies along altimetry tracks for estimating surface water storage variations in the congo basin. *Remote Sens.* **2021**, *13*, 3804. [CrossRef]
18. Alsdorf, D.; Han, S.C.; Bates, P.; Melack, J. Seasonal water storage on the Amazon floodplain measured from satellites. *Remote Sens. Environ.* **2010**, *114*, 2448–2456. [CrossRef]
19. Alsdorf, D.; Beighley, E.; Laraque, A.; Lee, H.; Tshimanga, R.; O'Loughlin, F.; Mahé, G.; Dinga, B.; Moukandi, G.; Spencer, R.G. Opportunities for hydrologic research in the Congo Basin. *Rev. Geophys.* **2016**. *54*, 378–409. [CrossRef]
20. Papa, F.; Frappart, F.; Güntner, A.; Prigent, C.; Aires, F.; Getirana, A.C.; Maurer, R. Surface freshwater storage and variability in the Amazon basin from multi-satellite observations, 1993–2007. *J. Geophys. Res. Atmos.* **2013**, *118*, 11951–11965. [CrossRef]
21. Salameh, E.; Frappart, F.; Papa, F.; Güntner, A.; Venugopal, V.; Getirana, A.; Prigent, C.; Aires, F.; Labat, D.; Laignel, B. Fifteen years (1993–2007) of surface freshwater storage variability in the ganges-brahmaputra river basin using multi-satellite observations. *Water* **2017**, *9*, 245. [CrossRef]
22. Frappart, F.; Seyler, F.; Martinez, J.M.M.; León, J.G.; Cazenave, A.; Leon, J.G.; Cazenave, A.; Cazenave, A. Floodplain water storage in the Negro River basin estimated from microwave remote sensing of inundation area and water levels. *Remote Sens. Environ.* **2005**, *99*, 387–399. [CrossRef]
23. Frappart, F.; Papa, F.; Santos Da Silva, J.; Ramillien, G.; Prigent, C.; Seyler, F.; Calmant, S.; da Silva, J.S.; Ramillien, G.; Prigent, C.; et al. Surface freshwater storage and dynamics in the Amazon basin during the 2005 exceptional drought. *Environ. Res. Lett.* **2012**, *7*, 044010. [CrossRef]
24. Frappart, F.; Bourrel, L.; Salazar, X.R.; Baup, F.; Baup, F.; Darrozes, J.; Pombosa, R. Spatio-temporal dynamics of the floods in the Guayas watershed (Ecuatorian Pacific Coast) using ENVISAT ASAR images. In Proceedings of the 2015 IEEE International Geoscience and Remote Sensing Symposium (IGARSS), Milan, Italy, 26–31 July 2015. [CrossRef]
25. Lee, H.; Beighley, R.E.; Alsdorf, D.; Jung, H.C.; Shum, C.K.; Duan, J.; Guo, J.; Yamazaki, D.; Andreadis, K. Characterisation of terrestrial water dynamics in the Congo Basin using GRACE and satellite radar altimetry. *Remote Sens. Environ.* **2011**, *115*, 3530–3538. [CrossRef]
26. Becker, M.; Papa, F.; Frappart, F.; Alsdorf, D.; Calmant, S.; da Silva, J.S.; Prigent, C.; Seyler, F. Satellite-based estimates of surface water dynamics in the Congo River Basin. *Int. J. Appl. Earth Obs. Geoinf.* **2018**, *66*, 196–209. [CrossRef]
27. Kitambo, B.; Papa, F.; Paris, A.; Tshimanga, R.; Frappart, F.; Calmant, S.; Elmi, O.; Fleischmann, A.; Becker, M.; Tourian, M.; et al. A long-term monthly surface water storage dataset for the Congo basin from 1992 to 2015. *Earth Syst. Sci. Data Discuss.* **2022**, 1–39. [CrossRef]
28. Prigent, C.C.; Prigent, C.C.; Prigent, C.C.; Jimenez, C.; Jimenez, C.; Bousquet, P.; Bousquet, P.; Bousquet, P.; Bousquet, P. Satellite-derived global surface water extent and dynamics over the last 25 years (GIEMS-2). *J. Geophys. Res.* **2020**, *125*, e2019JD030711. [CrossRef]
29. Crezee, B.; Dargie, G.C.; Ewango, C.E.; Mitchard, E.T.; Emba B, O.; Kanyama T, J.; Bola, P.; Ndjango, J.B.N.; Girkin, N.T.; Bocko, Y.E.; et al. Mapping peat thickness and carbon stocks of the central Congo Basin using field data. *Nat. Geosci.* **2022**, *15*, 639–644. [CrossRef]
30. Runge, J. The Congo River, Central Africa. In *Large Rivers: Geomorphology and Management*; Wiley Online Library: Hoboken, NJ, USA, 2008. [CrossRef]

31. Biddulph, G.E.; Bocko, Y.E.; Bola, P.; Crezee, B.; Dargie, G.C.; Emba, O.; Georgiou, S.; Girkin, N.; Hawthorne, D.; Jonay Jovani-Sancho, A.; et al. Current knowledge on the Cuvette Centrale peatland complex and future research directions. *Bois Forets Trop.* **2021**, *350*, 3–14. [CrossRef]
32. Dargie, G.C. Quantifying and Understanding the Tropical Peatlands of the Central Congo Basin. Ph.D. Thesis, University of Leeds, Leeds, UK, 2015.
33. Crezee, B.J. Spatial Distribution, Carbon Stocks and Diversity of Peat Swamp Forests in the Central Congo Basin. Ph.D. Thesis, University of Leeds, Leeds, UK, 2022.
34. Lampela, M.; Jauhiainen, J.; Kämäri, I.; Koskinen, M.; Tanhuanpää, T.; Valkeapää, A.; Vasander, H. Ground surface microtopography and vegetation patterns in a tropical peat swamp forest. *Catena* **2016**, *139*, 127–136. [CrossRef]
35. Apers, S.; Lannoy, G.D.; Lannoy, G.D.; Baird, A.; Baird, A.J.; Cobb, A.R.; Dargie, G.C.; del Aguila Pasquel, J.; del Aguila Pasquel, J.; Gruber, A.; et al. Tropical peatland hydrology simulated with a global land surface model. *J. Adv. Model. Earth Syst.* **2021**, *14*, e2021MS002784. [CrossRef]
36. Wang, Y.; Hess, L.L.; Filoso, S.; Melack, J.M. Understanding the radar backscattering from flooded and nonflooded Amazonian forests: Results from canopy backscatter modeling. *Remote Sens. Environ.* **1995**, *54*, 324–332. [CrossRef]
37. Hess, L.L.; Melack, J.M.; Affonso, A.G.; Barbosa, C.; Gastil-Buhl, M.; Novo, E.M. Wetlands of the Lowland Amazon Basin: Extent, Vegetative Cover, and Dual-season Inundated Area as Mapped with JERS-1 Synthetic Aperture Radar. *Wetlands* **2015**, *35*, 745–756. [CrossRef]
38. Rosenqvist, J.; Rosenqvist, A.; Jensen, K.; McDonald, K. Mapping of maximum and minimum inundation extents in the amazon basin 2014-2017 with ALOS-2 PALSAR-2 scan SAR time-series data. *Remote Sens.* **2020**, *12*, 1326. [CrossRef]
39. Rosenqvist, Å.; Birkett, C.M.; Rosenqvist Åand Birkett, C.M. Evaluation of JERS-1 SAR mosaics for hydrological applications in the Congo river basin. *Int. J. Remote Sens.* **2002**, *23*, 1283–1302. [CrossRef]
40. Rosenqvist, A.; Shimada, M.; Ito, N.; Watanabe, M. ALOS PALSAR: A pathfinder mission for global-scale monitoring of the environment. *IEEE Trans. Geosci. Remote Sens.* **2007**, *45*, 3307–3316. [CrossRef]
41. Garcin, Y.; Schefuß, E.; Dargie, G.C.; Hawthorne, D.; Lawson, I.T.; Sebag, D.; Biddulph, G.E.; Crezee, B.; Bocko, Y.E.; Ifo, S.A.; et al. Hydroclimatic vulnerability of peat carbon in the central Congo Basin. *Nature* **2022**, *612*, 277–282. [CrossRef]
42. Motohka, T.; Kankaku, Y.; Suzuki, S.; Shimada, M. Status of the advanced land observing satellite-2 (ALOS-2) and its follow-on L-band SAR mission. In Proceedings of the International Geoscience and Remote Sensing Symposium (IGARSS), Fort Worth, TX, USA, 23–28 July 2017. [CrossRef]
43. Yuan, T.; Lee, H.; Jung, H.C. Toward Estimating wetland water level changes based on hydrological sensitivity analysis of PALSAR backscattering coefficients over different vegetation fields. *Remote Sens.* **2015**, *7*, 3153. [CrossRef]
44. Landuyt, L.; Verhoest, N.E.; Van Coillie, F.M. Flood mapping in vegetated areas using an unsupervised clustering approach on sentinel-1 and-2 imagery. *Remote Sens.* **2020**, *12*, 3611. [CrossRef]
45. Funk, C.; Peterson, P.; Landsfeld, M.; Pedreros, D.; Verdin, J.; Shukla, S.; Husak, G.; Rowland, J.; Harrison, L.; Hoell, A.; et al. The climate hazards infrared precipitation with stations - A new environmental record for monitoring extremes. *Sci. Data* **2015**, *2*, 150066. [CrossRef]
46. Camberlin, P.; Barraud, G.; Bigot, S.; Dewitte, O.; Makanzu Imwangana, F.; Maki Mateso, J.C.; Martiny, N.; Monsieurs, E.; Moron, V.; Pellarin, T.; et al. Evaluation of remotely sensed rainfall products over Central Africa. *Q. J. R. Meteorol. Soc.* **2019**, *145*, 2115–2138. [CrossRef]
47. Santos, V.D.; Oliveira, R.A.J.; Datok, P.; Sauvage, S.; Paris, A.; Gosset, M.; Sánchez-Pérez, J.M. Evaluating the performance of multiple satellite-based precipitation products in the Congo River Basin using the SWAT model. *J. Hydrol. Reg. Stud.* **2022**, *42*, 101168. [CrossRef]
48. Fitts, C.R. *Groundwater Science*; Academic Press: Cambridge, MA, USA, 2012. [CrossRef]
49. Frappart, F.; Calmant, S.; Cauhopé, M.; Seyler, F.; Cazenave, A. Preliminary results of ENVISAT RA-2-derived water levels validation over the Amazon basin. *Remote Sens. Environ.* **2006**, *100*, 252–264. [CrossRef]
50. Kitambo, B.; Papa, F.; Paris, A.; Raphael, T.; Calmant, S.; Fleischmann, A.S.; Frappart, F.; Becker, M.; Tourian, M.J.; Prigent, C.; et al. A combined use of in situ and satellite-derived observations to characterize surface hydrology and its variability in the Congo River basin. *Hydrol. Earth Syst. Sci.* **2022**, *26*, 1857–1882. [CrossRef]
51. Yamazaki, D.; Ikeshima, D.; Tawatari, R.; Yamaguchi, T.; O'Loughlin, F.; Neal, J.C.; Sampson, C.C.; Kanae, S.; Bates, P.D. A high-accuracy map of global terrain elevations. *Geophys. Res. Lett.* **2017**, *44*, 5844–5853. [CrossRef]
52. Lee, J.S.; Wen, J.H.; Ainsworth, T.L.; Chen, K.S.; Chen, A.J. Improved sigma filter for speckle filtering of SAR imagery. *IEEE Trans. Geosci. Remote Sens.* **2009**, *47*, 202–213. [CrossRef]
53. Kim, D.; Lee, H.; Laraque, A.; Tshimanga, R.M.; Yuan, T.; Jung, H.C.; Beighley, E.; Chang, C.H. Mapping spatio-temporal water level variations over the central congo river using palsar scansar and envisat altimetry data. *Int. J. Remote Sens.* **2017**, *38*, 7021–7040. [CrossRef]
54. De Reu, J.; Bourgeois, J.; Bats, M.; Zwertvaegher, A.; Gelorini, V.; De Smedt, P.; Chu, W.; Antrop, M.; De Maeyer, P.; Finke, P.; et al. Application of the topographic position index to heterogeneous landscapes. *Geomorphology* **2013**, *186*, 39–49. [CrossRef]
55. Botsch, R.E. Chapter 12. Significance and Measures of Association. APLS 301 Scopes and Methods of Political Science Course, USCA 2011. Available online: https://polisci.usca.edu/apls301/Text/Chapter%2012.%20Significance%20and%20Measures%20of%20Association.htm (accessed on 9 June 2023).

56. Fu, L.L.; Alsdorf, D.; Morrow, R.; Rodriguez, E.; Mognard, N. SWOT: The Surface Water and Ocean Topography Mission Wide-Swath Altimetric Measurement of Water Elevation on Earth. *JPL Open Repository, V1*: Pasadena, CA, USA, 2012. Available online: https://hdl.handle.net/2014/41996 (accessed on 9 June 2023).
57. Biancamaria, S.; Lettenmaier, D.P.; Pavelsky, T.M. The SWOT Mission and Its Capabilities for Land Hydrology. In *Remote Sensing and Water Resources*; Cazenave, A., Champollion, N., Benveniste, J., Chen, J., Eds.; Springer International Publishing: Cham, Switzerland, 2016; pp. 117–147. [CrossRef]
58. Medasani, S.; Reddy, G.U. Analysis and Evaluation of Speckle Filters by Using Polarimetric Synthetic Aperture Radar Data Through Local Statistics. In Proceedings of the 2nd International Conference on Electronics, Communication and Aerospace Technology, ICECA 2018, Coimbatore, India, 29–31 March 2018. [CrossRef]

Disclaimer/Publisher's Note: The statements, opinions and data contained in all publications are solely those of the individual author(s) and contributor(s) and not of MDPI and/or the editor(s). MDPI and/or the editor(s) disclaim responsibility for any injury to people or property resulting from any ideas, methods, instructions or products referred to in the content.